

1 **Performance of AIRS ozone retrieval over the central Himalayas: Case studies of biomass**  
2 **burning, downward ozone transport and radiative forcing using long-term observations**

3

4

5 Prajwal Rawat<sup>1,5</sup>, Manish Naja<sup>1</sup>, Evan Fishbein<sup>2</sup>, Pradeep K. Thapliyal<sup>3</sup>, Rajesh Kumar<sup>4</sup>, Piyush  
6 Bhardwaj<sup>4</sup>, Aditya Jaiswal<sup>1</sup>, Sugriva N. Tiwari<sup>5</sup>, Sethuraman Venkataramani<sup>6</sup>, Shyam Lal<sup>6</sup>

7

8

9

10 <sup>1</sup> Aryabhata Research Institute of Observational Sciences (ARIES), Nainital, 263001, India

11 <sup>2</sup> NASA Jet Propulsion Laboratory, Pasadena, CA 91109, USA

12 <sup>3</sup> Space Applications Centre, ISRO, Ahmedabad 380015, India

13 <sup>4</sup> National Center for Atmospheric Research (NCAR) Boulder, CO 80307, USA

14 <sup>5</sup> DDU Gorakhpur University, Gorakhpur 273009, India

15 <sup>6</sup> Physical Research Laboratory (PRL), Ahmedabad, 380009, India

16

17

18

19

20 **Corresponding author:** Manish Naja ([manish@aries.res.in](mailto:manish@aries.res.in))

21

22

23

24

25

26 **Short Summary:**

27 Satellite based ozone observations have gained wide importance due to their global coverage.  
28 However, satellite retrieved products are indirect and need to be validated, particularly over  
29 mountains. Here, ozonesondes launched from a Himalayan site are utilized to assess the AIRS  
30 ozone retrieval. AIRS is shown to overestimate ozone in the upper troposphere and lower  
31 stratosphere, while the differences with ozonesonde are lower in the middle troposphere and  
32 middle stratosphere.

33

34

35

36

37

38

39

40

41

42

43

44

45

46

47

48

49

50

51 **Abstract**

52 Data from 242 ozonesondes launched from ARIES Nainital (29.40° N, 79.50° E, and 1793 m  
53 elevation) are used to evaluate the Atmospheric Infrared Sounder (AIRS) version 6 ozone profiles  
54 and total column ozone during the period 2011-2017 over the central Himalaya. The AIRS ozone  
55 products are analyzed in terms of retrieval sensitivity, retrieval biases/errors, and ability to retrieve  
56 the natural variability of columnar ozone, which has not been done so far from the Himalayan  
57 region having complex topography. For a direct comparison, averaging kernels information is used  
58 to account for the sensitivity difference between the AIRS and ozonesonde data. We show that  
59 AIRS has lower differences with ozonesonde in the lower and middle troposphere and stratosphere  
60 with nominal underestimations of less than 20%. However, in the upper troposphere and lower  
61 stratosphere (UTLS), we observe a considerable overestimation of the magnitude, as high as 102%.  
62 The weighted statistical error analysis of AIRS ozone shows higher positive bias and standard  
63 deviation in the upper troposphere of about 65% and 25%, respectively. Similar to AIRS, Infrared  
64 Atmospheric Sounding Interferometer (IASI) and Cross-track Infrared Sounder (CrIS) are also  
65 able to produce ozone peak altitudes and gradients successfully. However, the statistical errors are  
66 again higher in the UTLS region that are likely related to larger variability of ozone, lower ozone  
67 partial pressure and inadequate retrieval information on the surface parameters. Furthermore,  
68 AIRS fails to capture the monthly variation of the total ozone column, with a strong bimodal  
69 variation, unlike unimodal variation seen in ozonesonde and Ozone Monitoring Instrument (OMI).  
70 In contrast, the UTLS and the tropospheric ozone columns are in reasonable agreement. Increases  
71 in the ozone values by 5 - 20% after biomass burning and during events of downward transport  
72 are captured well by AIRS. Ozone radiative forcing (RF) derived from total column ozone using  
73 ozonesondes data (4.86 mW/m<sup>2</sup>) matches well with OMI (4.04 mW/m<sup>2</sup>), while significant RF  
74 underestimation is seen in AIRS (2.96 mW/m<sup>2</sup>). The fragile and complex landscapes of the  
75 Himalayas are more sensitive to global climate change and establishing such biases and error  
76 analysis of space-borne sensors will help study the long-term trends and estimate accurate radiative  
77 budgets.

78

79

80

81

82 **1. Introduction**

83 Atmospheric ozone is an essential trace gas that plays a crucial role in the atmospheric oxidizing  
84 chemistry, air quality, and earth's radiative budget. The stratospheric ozone absorbs harmful solar  
85 ultraviolet radiation and protects biological life on earth, whereas tropospheric ozone, being a  
86 secondary air pollutant (Logan et al., 1985; Pitts and Pitts, 1997; Pierce et al., 2009; Monks et al.,  
87 2015; Lelieveld et al., 2018) and greenhouse gas, contributes to global warming and can harm  
88 human health and crops when present in higher concentrations near the surface (Fishman et al.,  
89 1979; Ebi and McGregor 2008; Lal et al., 2017). Different radiative forcing of ozone from the  
90 stratosphere (cooling) to the troposphere (heating) (Lacis et al., 1990; Forster et al., 2007; Wang  
91 et al., 1993; Hegglin et al., 2015) demonstrate its potential importance as an atmospheric climate  
92 gas (Shindell et al., 2012; Thornhill et al., 2021). Hence, information regarding precise long-term  
93 variability in global ozone distribution is vital for better characterizing atmospheric chemistry and  
94 global climate changes (McPeters et al., 1994; Kim et al., 1996; Myhre et al., 2017).

95

96 In recent decades, observations of ozone from space-borne sensors (microwave limb sounding,  
97 UV-VIS, and IR) have become an increasingly robust tool for global and higher temporal  
98 monitoring (Fishman et al., 1986; Munro et al., 1998; Bhartia et al., 1996; Foret et al., 2014). This  
99 increases our ability to analyze various influences of human activities on the atmospheric chemical  
100 composition, including ozone, study their long-term impact on climate (Fishman et al., 1987; Fry  
101 et al., 2012; Tarasick et al., 2019; Thornhill et al., 2021), and estimate reliable radiative budgets  
102 (Hauglustaine and Brasseur 2001; Gauss et al., 2003; Aghedo et al., 2011). However, the space-  
103 based sensors are indirect and measure the atmospheric composition based upon specific  
104 algorithms utilizing radiative transfer models and a-priori information. Hence, the retrieval outputs

105 need to be evaluated with certain reference instruments for establishing the credibility and better  
106 utilization of space-borne data.

107

108 The Himalayas, a complex terrain region, has the largest abundance of ice sheets outside polar  
109 regions that impacts global/regional radiative budgets and climate pervasively (e.g., Lawrence and  
110 Lelieveld, 2010; Cristofanelli et al., 2014; Zhang et al., 2015). Very sparse in-situ and ground-  
111 based observations in this region, along with inadequate information on the surface parameters,  
112 makes it difficult to retrieve atmospheric composition from space-borne instruments. This is  
113 because the ozone weighting function, a measure of the retrieval sensitivity and a fundamental  
114 retrieval component, depends upon various atmospheric parameters like surface temperature,  
115 surface emissivity, and terrain height (Rodgers et al., 1976, 1990; Bai et al., 2014), which is not  
116 uniform over the foot-print size of the AIRS (~ 13 km x 13 km) over the Himalayas. Usually, the  
117 ozone weighting function has a shorter integrating path over the elevated terrain regions, which  
118 follows a smaller weighting function and provides lesser sensitivity and higher errors in the final  
119 retrievals (Coheur et al., 2005; Bai et al., 2014).

120

121 The Atmospheric Infrared Sounder (AIRS) onboard the Aqua satellite has been providing reliable  
122 vertical profiles of ozone, temperature, water vapor, and other trace gases globally twice a day  
123 since 2002. Numerous validation studies of AIRS retrieved ozone have been carried out for  
124 different versions since it started operating (2002). For example, Bian et al. (2007) studied AIRS  
125 version 4 over Beijing and discussed the potential agreements (within 10%) between AIRS and  
126 ozonesonde (GPSO3) ozone, particularly in the upper troposphere and lower stratosphere (UTLS)  
127 region with the capability of AIRS to identify various Stratosphere-Troposphere Exchange (STE)

128 and transient convective events. Similarly, a study over Boulder and Lauder by Monahan et al.  
129 (2007) using a similar AIRS version showed despite the larger biases in the lower and middle  
130 tropospheric region, the retrieval algorithm captures the ozone variability very effectively with a  
131 positive correlation of more than 70%. However, that study suggested a need for tropopause-  
132 adjusted coordinates in the a-priori profiles. Both these studies (Bian et al., 2007; Monahan et al.,  
133 2007) show larger biases in AIRS ozone in the lower and middle tropospheric regions; however,  
134 shifts in retrieval biases and errors were seen towards the UTLS region in version 5 (Divakarla et  
135 al., 2008), apart from significant improvements in the lower troposphere. The retrieval  
136 methodology has also changed significantly between V4 and V5. Version 4 or earlier used  
137 regression retrieval as the first guess in physical retrieval, while later versions used a climatology-  
138 based first guess for the physical retrieval based on other works (McPeters et al., 2007). Also,  
139 radiative transfer models, selected channel sets, and clarified quality indicators have been modified  
140 and improved in all successive versions.

141  
142 The AIRS ozone retrieval in V5 has improved significantly with retrieval biases and root mean  
143 square error (RMSE) less than 5% and 20%, respectively (Divakarla et al., 2008), over the tropical  
144 regions. However, there is not much discussion and studies of the assessment for AIRS ozone over  
145 the Himalayas' complex terrain, where retrieval is expected to be erroneous due to large surface  
146 variability within its footprint. Also, most of the previous studies (Bian et al., 2007; Divakarla et  
147 al., 2008; Pittman et al., 2009) did not utilize the averaging kernels information of the AIRS that  
148 is vital for satellite evaluation.

149

150 Here, the evaluation of AIRS version 6, which entirely depends upon the infra-red (IR)  
151 observations after the failure of the AMSU sensor, is presented in terms of statistical analysis and  
152 ability to retrieve the natural variability of ozone at various altitudes over the central Himalayan  
153 region using in-situ ozonesonde observations convolved with AIRS averaging kernels.  
154 Additionally, the present study assessed the AIRS retrieval algorithm using IASI and CrIS radiance  
155 information for one year. AIRS columnar ozone (i.e., total, UTLS, and tropospheric columns) is  
156 also assessed with ozonesonde, OMI, and Microwave Limb Sounder (MLS) observations. AIRS  
157 has a long-term data set for ozone and meteorological parameters, establishing such biases and  
158 error analysis is essential to make meaningful use of its data to characterize the Himalayan  
159 atmosphere, study the trends, radiative budgets, perform the model evaluation and data  
160 assimilation over this region.

161

## 162 **2 Data and Methodology**

### 163 **2.1 Data Description**

#### 164 **2.1.1 AIRS**

165 Atmospheric Infrared Sounder (AIRS) onboard Aqua satellite, in the sun synchronous polar orbit  
166 at 705 km altitude, is a hyperspectral thermal infrared grating spectrometer with equatorial  
167 crossings at ~13:30 local time (LT). It is a nadir scanning sensor that was deployed in orbit on  
168 May 4, 2002. AIRS, along with its partner microwave instrument, the Advanced Microwave  
169 Sounding Unit (AMSU-A), represents the most advanced atmospheric sounding system placed in  
170 space using cutting-edge infrared and microwave technologies. These instruments together  
171 observe the global energy cycles, water cycles, climate variations, and greenhouse gases, however,  
172 after AMSU failure, the retrieval now mostly depends upon the AIRS IR observations. The AIRS

173 infrared spectrometer acquires 2378 spectral samples at resolutions ( $\lambda/\Delta\lambda$ ) ranging from 1086 to  
174  $1570\text{ cm}^{-1}$ , in three bands:  $3.74\text{ }\mu\text{m}$  to  $4.61\text{ }\mu\text{m}$ ,  $6.20\text{ }\mu\text{m}$  to  $8.22\text{ }\mu\text{m}$ , and  $8.8\text{ }\mu\text{m}$  to  $15.4\text{ }\mu\text{m}$   
175 (Fishbein et al., 2003; Pagano et al., 2003). The independent channels of AIRS permit retrieval of  
176 various atmospheric states and constituents depending upon their corresponding spectral response,  
177 even in the presence of a 90% cloud fraction (Susskind et al., 2003; Maddy and Barnet, 2008). In  
178 this study, we have used Level 2 Support physical products of AIRS (AIRS2SUP). The AIRS2SUP  
179 files (~240 granules/day) possess extra information over the standard AIRS files, e.g., information  
180 on averaging kernel and degree of freedom, including vertical profiles at 100 pressure levels,  
181 against just 28 in the standard product.

182

183 The support product profiles contain 100 levels between 1100 and 0.016 mbar. While it has a  
184 higher vertical resolution, the vertical information content is no greater than the standard product.  
185 The information on averaging kernels and degree of freedoms (DOFs) is utilized to understand the  
186 retrieved products more comprehensively. The DOFs of ozone, a measure of significant eigen  
187 functions used in the AIRS retrieval, have an average value of 1.36 over the tropical latitude band  
188 (Maddy and Barnet 2008) (Table S1), while over the balloon collocated region, an average DOFs  
189 of 1.62 is observed (Figure S1). In the present study, the AIRS data is flagged as best quality when  
190 the cloud fraction is less than 80%, and the degrees of freedom (DOF) are greater than 0.04.  
191 However, analysis of cloud fraction over our collocated region shows (Figure S2) only 7% of  
192 observations during 2011 - 2017 had a cloud fraction of more than 80%.

193

194

195



196 **2.1.2 IASI (NOAA/CLASS)**

197 The Infrared Atmospheric Sounding Interferometer (IASI) onboard MetOp satellites, with a  
198 primary focus on meteorology than climate and atmospheric chemistry monitoring, is a nadir  
199 viewing Michelson interferometer (Clerbaux et al., 2007). The first MetOp satellite was launched  
200 in October 2006 (MetOp-A), and IASI was declared operational in July 2007. MetOp is a polar  
201 sun-synchronous satellite having descend and ascend nodes at 09:30 and 21:30 LT, respectively.  
202 IASI measures in the IR part of the EM spectrum at a horizontal resolution of 12 km at nadir up to  
203 40 km over a swath width of about 2,200 km. IASI covers an infra-red spectral range between 3.7  
204 to 15.4  $\mu\text{m}$  with a total of 8461 spectral channels, out of which 53 channels around 9.6  $\mu\text{m}$  are  
205 utilized for ozone retrieval. IASI level 2 ozone products provided by NOAA National  
206 Environmental Satellite Data and Information Service (NESDIS) Center for Satellite Application  
207 and Research (STAR) are used in this study. The IASI (NOAA/CLASS) ozone product is retrieved  
208 based on the AIRS algorithm and has various quality control flags (Table S2). Only QC=0 data  
209 which represents a successful IR ozone retrieval, is used.

210

211 **2.1.3 CrIS/ATMS (NUCAPS)**

212 The Cross-track Infrared Sounder (CrIS) and Advanced Technology Microwave Sounder (ATMS)  
213 onboard the Suomi NPP satellite were launched in 2011 to feature the high spectral-resolution  
214 (“hyperspectral”) observations of earth’s atmosphere. The CrIS instrument is an advanced Fourier  
215 transform spectrometer with an ascending node 13:30 LT and flies at a mean altitude of 824 km  
216 and performs fourteen orbits per day. It measures high-resolution IR spectra in the spectral range  
217 650 - 2550  $\text{cm}^{-1}$  with a total of 1305 channels. The ATMS is a microwave sounder with a total of  
218 22 channels ranging from 23 to 183 GHz. These two instruments, CrIS and ATMS, operate in an

219 overlapping field-of-view (FOV) formation, with ATMS FOVs re-sampled to match the location  
220 and size of the 3×3 CrIS FOVs for retrieval under clear to partly cloudy conditions. Here the  
221 NUCAPS algorithm-based ozone product of CrIS is utilized. The NOAA Unique CrIS/ATMS  
222 Processing System (NUCAPS) is a heritage algorithm developed by the STAR team based on the  
223 AIRS retrieval algorithm (Susskind et al., 2003, 2006). The NOAA implemented NUCAPS  
224 algorithm is a modular architecture that was specifically designed to be compatible with multiple  
225 instruments. The same retrieval algorithms are currently used to process the AIRS/AMSU suite  
226 (operations since 2002), the IASI/AMSU/MHS suite (operational since 2008), and now the  
227 CrIS/ATMS suite (approved for operations in January 2013). Here again, various quality controls  
228 for retrieved data are provided by the NUCAPS science algorithm team, and we used QC=0 for  
229 lesser discrepancies in our evaluation (Table S2). These research products follow a similar retrieval  
230 algorithm as developed by the AIRS science team, which gives us further opportunity to assess the  
231 AIRS retrieval algorithm for IASI and CrIS radiances.

232

#### 233 **2.1.4 Ozonesonde**

234 Electrochemical concentration cell (ECC) ozonesondes and GPS-radiosondes have been launched  
235 from the Aryabhata Research Institute of Observational Sciences (ARIES) (29.4° N, 79.5° E, and  
236 1793 m elevation) Nainital (Figure 1), a high-altitude site in central Himalaya, since 2011 (Ojha  
237 et al., 2014; Rawat et al., 2020), the only facility in the Himalayan region having regular  
238 launchings. ECC ozonesonde relies on the oxidation reaction of ozone with potassium iodide (KI)  
239 solution (Komhyr et al., 1967, 1995) to measure ozone partial pressure in the ambient atmosphere.  
240 The typical vertical resolution of ozonesonde is about 100 - 150 m and has a precision of better  
241 than  $\pm 3 - 5 \%$  with an accuracy of about  $\pm 5 - 10 \%$  up to 30 km altitude under standard operating

242 procedures (Smit et al., 2007). The ozonesonde is connected to iMet-radiosonde via a V7 electronic  
243 interface, where radiosonde consists of GPS, PTU, and a transmitter to transmit signals to the  
244 ground. Due to higher accuracy and in-situ measurement, ozonesonde has been widely used  
245 worldwide for satellite and model validation (Divakarla et al., 2008; Nassar et al., 2008; Monahan  
246 et al., 2007; Kumar et al., 2012a, 2012b; Dufour et al., 2012; Verstraeten et al., 2013; Boynard et  
247 al., 2016; Rawat et al., 2020). Both the ascending and descending data were recorded by  
248 ozonesonde, however, due to time lag in descending records, only ascending data is utilized (Lal  
249 et al., 2013, 2014; Ojha et al., 2014). The data is collected at the interval of about 10 meters which  
250 is averaged over 100 meters interval using a  $3\sigma$  filter that removes the outlier values (Srivastava  
251 et al., 2015; Naja et al., 2016).

252

### 253 **2.1.5 Other Auxiliary Data**

254 Additionally, collocated and concurrent OMI and MLS observations are also used to study the  
255 tropospheric ozone, UTLS, and total ozone column due to their reasonable sensitivity and well-  
256 validated retrievals (Veefkind et al., 2006; Ziemke et al., 2006; Fadnavis et al., 2014; Wang et al.,  
257 2021). The tropospheric ozone column obtained from OMI and MLS is based on the residual  
258 method, which depends upon the collocated difference between the MLS stratospheric ozone  
259 column and OMI total ozone column, which is described in detail by Ziemke et al. (2006).  
260 Furthermore, the MLS version 4 data is utilized for the UTLS column above 261 hPa due to its  
261 credibility in this range for scientific applications (Livesey et al., 2013; Schwartz et al., 2015).  
262 Moreover, for fair statistical analysis between ozonesonde and MLS ozone profile, Gaussian  
263 smoothing is applied to ozonesonde with full width at half maximum equal to typical upper  
264 tropospheric vertical resolution ( $\sim 2 - 4$  km) of MLS (Livesey et al., 2013). The best quality data

265 of MLS with data flags, i.e., status=even, quality > 0.6, and convergence < 1.18, is utilized (Ziemke  
266 et al., 1998; Barre et al., 2012). However, a slightly different collocation criterion of 3°×3° grid  
267 box and daytime collocation is utilized for MLS in this work due to coarser resolution and to get  
268 sufficient matchups.

269

## 270 **2.2 Methods of Analysis**

271 The balloon launch time is mostly around 12:00 IST (Indian Standard Time, which is 5.5 hours  
272 ahead of GMT). The Aqua satellite comes over the India around 1:30 pm and 1:30 am IST. Hence  
273 for collocation, only noontime (ascending) data (or ± 3 hours of balloon launch) with 1°×1° spatial  
274 collocation were chosen in this evaluation. However, for some days, there was no noontime  
275 granule in AIRS retrieval (nearly 35 out of total 242 soundings), then we used a loose collocation  
276 of ±1 day. However, no significant changes were seen after such flexible collocation. Most of the  
277 ozonesondes have burst altitudes near 10 hPa, hence AIRS ozone profiles are evaluated from  
278 surface to 10 hPa.

279

280 Although suitable collocation criteria have been defined for a fair comparison, still different  
281 vertical resolutions of the two data sets (ozonesonde ~100 m and AIRS ~1-5 km) make the  
282 meaningful comparison difficult (Maddy and Barnett, 2008; Verstraeten et al., 2013; Boynard et  
283 al., 2016). The difference in vertical resolution and retrieval sensitivity must be accounted for a  
284 meaningful comparison. Though there is no perfect way to remove the error arising from the  
285 different vertical resolutions of the two measurements, still utilizing the averaging kernel  
286 smoothing or Gaussian smoothing, the error is minimized. Various groups have used the satellite  
287 averaging kernels smoothing to compare satellite measurements with ozonesonde (Zhang et al.,

288 2010; Verstraeten et al., 2013; Boynard et al., 2016, 2018), while Gaussian smoothing (Wang et  
 289 al., 2020) and broad layer columns (Nalli et al., 2017) are also utilized. In the present analysis,  
 290 averaging kernel smoothing is utilized. First, ozonesonde data were interpolated at all AIRS  
 291 Radiative Transfer Algorithm (RTA) layers from surface to burst altitude, then ozonesonde  
 292 profiles were smoothed according to the AIRS averaging kernel and a-priori profile (ML  
 293 climatology), leading to a vertical profile [ozonesonde (AK)] representing what AIRS would have  
 294 measured for the same ozonesonde sampled atmospheric air mass in the absence of any other error  
 295 affecting satellite observations. According to Rodgers and Connor (2003), the smoothing of the  
 296 true state can be characterized as follows:

$$297 \quad X_{est} = X_0 + A'(X_{sonde} - X_0) \quad (1)$$

298 The AIRS provides averaging kernels information at 9 pressure levels (Figure 2b) whereas the  
 299 AIRS RTA has 100 pressure levels. So following ozone vertices (Table S3) and formulating  
 300 trapezoid matrix (Figure 2a, the details regarding the calculation of trapezoid matrices are given  
 301 in AIRS/AMSU/HSB Version 6 Level 2 Product Levels, Layers and Trapezoids), we convert 9  
 302 levels AIRS averaging kernels to 100 levels averaging kernels using following defined operation.

$$303 \quad A' = F \times A_{trapezoid} \times F' \quad (2)$$

304 Where  $A_{trapezoid}$  and  $F$  are averaging kernel matrices and trapezoid matrices ( $F'$  is pseudo-inverse  
 305 of  $F$ ).  $A_{trapezoid}$  is a given product, while  $F$  is calculated for given ozone vertices (Table S3).

306 Further, in the thermal IR spectrum, the contribution of ozone or any other trace gas towards  
 307 emission/absorption of IR radiation in the radiative transfer equation depends on the exponent of  
 308 layer integrated column amounts (Maddy and Barnet, 2008). Hence logarithmic changes in layer

309 column density are more linear than absolute changes. So logarithmic equations are used instead  
310 of Eq. 1 for smoothing ozonesonde data in the present study.

$$311 \quad \ln (X_{\text{est}}) = \ln (X_0) + A' \{ \ln (X_{\text{sonde}}) - \ln (X_0) \} \quad (3)$$

312 Where  $X_{\text{est}}$ ,  $X_{\text{sonde}}$ , and  $X_0$  are smooth ozonesonde or ozonesonde (AK), true ozonesonde, and first  
313 guess (ML climatology) profiles, respectively.

314 More details on the calculation of averaging kernels can be found in AIRS documents  
315 (AIRS/AMSU/HSB Version 6 Level 2 Product Levels, Layers and Trapezoids) or in available  
316 literature (Maddy and Barnett, 2008; Irion et al., 2018). A typical averaging kernels matrix and  
317 other parameters are shown in Figure 2. Figure 2a shows a typical trapezoid matrix, Figure 2b  
318 shows the averaging kernels at 9 pressure levels, Figure 2c shows constructed averaging kernels  
319 at 100 RTA layers, and Figure 2d shows an example of the different ozone profiles convolved with  
320 AKs on 15 June 2011 over the observation site.

321

### 322 **2.3 Statistical Analysis**

323 The error analysis for AIRS retrieval with interpolated and smoothed ozonesonde is based on Nalli  
324 et al. (2013, 2017). Bias, root mean squared error (RMSE), and standard deviation (STD) are  
325 studied at various RTA vertical levels from the surface to 10hPa over the Himalayan region. The  
326 finer spatio-temporal collocation utilized here has further minimized the uncertainty and error in  
327 the evaluation. Since the observation site (29.4° N, 79.5° E) is at a latitude lower than 45°; hence  
328 there is a lesser overlap of satellite passes, and mostly a few nadir scans are close to the observation  
329 site (mostly daytime granules in the range of 75 to 85). Hence all the daytime observations of

330 AIRS are close to  $\pm 3$  hours of temporal collocation to the ozonesonde launch and possess a lesser  
 331 chance of time mismatch.

332  
 333 Given the collocated ozone mixing ratio profiles for satellite, ozonesonde (AK), and in-situ truth  
 334 (ozonesonde) observations, the statistical errors are calculated as follows -

335  
 336 
$$\text{RMSE} (\Delta O_l) = \sqrt{\frac{\sum_{j=1}^{j=n} W_{l,j} \times (\Delta O_{l,j})^2}{\sum_{j=1}^{j=n} W_{l,j}}} \quad (4)$$

337  
 338 
$$\text{Bias} (\Delta O_l) = \frac{\sum_{j=1}^{j=n} W_{l,j} \times (\Delta O_{l,j})}{\sum_{j=1}^{j=n} W_{l,j}} \quad (5)$$

339 Here  $l$  runs over different RTA layers and  $j$  runs for all collocated profiles,  $\Delta O_{l,j}$  the fractional  
 340 deviation is taken to be the absolute deviation divided by the observed value. Where  $\Delta O_{l,j} =$   
 341  $\left(\frac{O_{l,j}^R - O_{l,j}^T}{O_{l,j}^T}\right)$ ,  $O^T$  and  $O^R$  are ozonesonde/ozonesonde (AK) and satellite retrieved ozone mixing ratio,  
 342 respectively.  $W_{l,j}$  is the weighting factor and assumes one of three forms  $W_0 = 1$ ,  $W_1 = O^R$  and  $W_2$   
 343  $= (O^R)^2$  and for ozone to minimize skewing impact due to large variation in mixing ratio at different  
 344 altitudes, we have used the  $W_2$  weight factor as suggested by other sounder science team (Nalli et  
 345 al., 2013, 2017). The Standard deviation (STD) is then calculated by the square root of difference  
 346 between RMSE and biases square at different RTA levels. Further to check the strength of the  
 347 linear relationship between the satellites retrieved data and ozonesonde data the square of  
 348 Pearson's correlation coefficient is also calculated.

349  
 350

## 351 **2.4 Estimation of Columnar Ozone**

352 The total column ozone (TCO) from ozonesonde is calculated by integrating the ozone mixing  
353 ratio from the surface to burst altitude and then adding residual ozone above burst altitude. Here  
354 the residual ozone is obtained from satellite-derived balloon-burst climatology (BBC) (McPeters  
355 et al., 1997). The discrete integration for calculation of total ozone column (DU) between defined  
356 boundaries is performed as follows:

$$357 \quad \text{Total column ozone} = 10^7 \times \left( \frac{RT_o}{g_o P_o} \right) \times \sum_{j=1}^{j=n} 0.5 \times (VMR[i] + VMR[i + 1]) \times (P[i] - P[i + 1]) \quad (6)$$

358

359 Where P is ambient pressure in hPa, VMR volume mixing ratio of ozone in ppbv, R (= 287.3 JKg<sup>-1</sup>  
360 K<sup>-1</sup>) gas constant, g<sub>o</sub> (= 9.88 ms<sup>-2</sup>), P<sub>o</sub> (= 1.01325×10<sup>5</sup> Pa) and T<sub>o</sub> (= 273.1 K) standard  
361 temperature.

362 The UTLS ozone column (DU) is also calculated using Eq. (6), where the UTLS region is defined  
363 between 400 hPa to 70 hPa (Bian et al., 2007). Additionally, the tropospheric ozone column (DU)  
364 is calculated for ozonesonde utilizing Eq. (6) with boundaries from the surface to the tropopause.  
365 The tropopause height from balloon-borne observations is estimated using the lapse rate method  
366 as well as the AIRS-derived tropopause is used and shown in Figure 3. However, for OMI and  
367 MLS tropospheric ozone residual method is used, which calculates the tropospheric ozone column  
368 by subtracting the OMI total column from MLS stratospheric ozone column (Hudson et al., 1998;  
369 Ziemke et al., 2006).

370

371

372

373



### 374 **3. Results and Discussion**

#### 375 **3.1 Ozone Distribution Along Balloon Trajectory: Ozonesonde and AIRS**

376 The distributions of ozone along the balloon tracks obtained using all ozone soundings data during  
377 four seasons are shown in Figure 4. The nearest swath of AIRS ozone observations is interpolated  
378 to the balloon locations and altitudes. Altitude variations of the balloon along longitude are  
379 shown in Figure S3. The balloons drift to a very long-distance during winter, followed by autumn  
380 and spring. During these seasons, balloons often reach Nepal also. The wind reversal took place  
381 during the summer-monsoon when the balloon drifts towards IGP regions (Figure 4). The  
382 distributions of ozone from AIRS are more-or-less similar to the distributions those from  
383 ozonesonde. Here, the ozone variations are reflecting in terms of spatial as well as vertical  
384 distributions. The bias and coefficient of determination ( $r^2$ ) between ozonesonde and AIRS ozone  
385 are studied along the longitude and latitude (Figures S3 and S4). Lower biases (lesser than 10%)  
386 and higher  $r^2$  are seen in the lower and middle troposphere. The poor correlation ( $<0.4$ ) and larger  
387 biases of up to 28% are seen at certain longitudes that are associated with higher altitudes ( $> 20$   
388 km). Around the balloon launch site (Nainital, 79.45 E) highest  $r^2$  score of 0.98 and low bias of  
389 1.4% are observed, which remain higher ( $r^2$ ) and lower (bias) up to 80° E (Figure S3).

390

391

#### 392 **3.2 Ozone Soundings and AIRS Ozone Profiles**

393 Figure 5 shows the average monthly ozone profiles for collocated observations of ozonesonde and  
394 AIRS, respectively, during seven-year periods. The ozonesonde convolved with AIRS averaging  
395 kernels [ozonesonde (AK)] and AIRS a-priori are also compared. The value of percentage  
396 difference between ozonesonde and AIRS ozone at 706, 617, 496, 103, 29, and 14 hPa altitudes

397 are shown in figure 5, and the zoomed variations in the lower tropospheric ozone (surface to 200  
398 hPa) are also presented in the insets. AIRS slightly (~10%) underestimates ozone in the lower  
399 troposphere during most of the months, except the summer-monsoon (June-August), where an  
400 overestimation of up to 20% is observed. In the middle troposphere, around 300 hPa, an  
401 underestimation in the range of 1 - 17% is seen for all months with an approaching tendency of  
402 ozonesonde (AK) towards the true ozonesonde profiles. However, near the tropopause region,  
403 AIRS retrievals considerably overestimate ozone by up to 102%. The overestimation was  
404 highest for the winter season (82 - 102%), followed by the spring, and autumn, while lowest for  
405 the summer-monsoon season (10 - 27%). In the stratosphere, where the sensitivity of AIRS is  
406 higher (Figure 2c), the ozonesonde and AIRS differences were relatively lesser. Additionally,  
407 AIRS retrieval shows an underestimation of 5 - 21% in this altitude region.

408  
409 As expected, the difference between ozonesonde and AIRS is significantly reduced (Table 1) after  
410 applying the averaging kernel or accounting for the sensitivity difference. This reduction was more  
411 notable for the summer monsoon period near the tropopause, where the difference reduced from  
412 92% to 19%, providing an improvement of 72%. The improvement is as high as 100% on a  
413 monthly basis. Additionally, relative difference profiles were also analyzed for individual  
414 soundings as well for the different seasons (Figure S5). Higher differences of about 150% between  
415 AIRS and ozonesonde ozone observations were seen in the upper troposphere and lower  
416 stratospheric (UTLS) region. The higher difference during winter and spring between these  
417 observations in the UTLS region could be due to recurring ozone transport via tropopause folding  
418 over the observation site. Such events may remain undetected by AIRS due to lower vertical  
419 resolution leading to the missing of some tropopause folding events at lower altitudes (Figure 3).

420 However, in the lower troposphere, larger differences between ozonesonde and AIRS during  
421 summer-monsoon are seen, which are due to low ozone and frequent cloudy conditions leading to  
422 poor retrieval. The arrival of cleaner oceanic air during the south-west monsoon (or summer  
423 monsoon) brings ozone-poor air and frequent cloudy conditions over northern India that weakens  
424 the photochemical ozone production (Naja et al., 2014; Sarangi et al., 2014). Moreover, in the  
425 lower troposphere, the limited sensitivity of hyperspectral satellite instruments has a significant  
426 contribution from the a-priori information, which is also observed for AIRS retrieval (Figure 5).

427

428 Figure 6 shows the yearly time series analysis of the average ozone mixing ratio at four defined  
429 layers, characterizing the middle troposphere (600 - 300 hPa), the upper troposphere (300 - 100  
430 hPa), lower stratosphere (100 - 50 hPa), and middle stratosphere (50 - 10 hPa) respectively. A  
431 prominent seasonality was seen in the time series throughout the years, which is quite clear in the  
432 upper troposphere (300 - 100 hPa). The ozone seasonality contrast reflects the influence of  
433 summer-monsoon and winter seasons. The seasonality contrast is similar between AIRS and  
434 ozonesonde measurements, while a reversal of ozone seasonality is observed in the middle  
435 stratospheric region compared to other layers. The opposite seasonality of the middle stratospheric  
436 region is primarily due to dominant circulations, variation of solar radiation and dynamics. Total  
437 column water vapor is also shown in Figure 6 that shows a tendency of anti-correlation with ozone  
438 in the 300 - 100 hPa region.

439

440 We have also estimated the monsoon index by the difference between zonal (U) wind (MERRA-  
441 2) at 850 hPa over the Arabian Sea (40 E – 80 E, 5 N – 15 N) and over the central Indian landmass  
442 (70 E - 90 E, 20 N – 30 N) as done by Wang et al. (2001).

443 In general, the positive values of the monsoon index correspond to strong monsoons and negative  
444 values correspond to weak monsoon periods (Wang et al., 2001). During the weak monsoon, there  
445 is relatively drier air, lower cloud cover and higher surface temperature compared to the strong  
446 monsoon period (Lu et al., 2018). We observed a tendency of lower annual average ozone (from  
447 ozonesonde and AIRS measurements) during greater (positive) monsoon index and higher annual  
448 average ozone during lower (negative) monsoon index. Lu et al. (2018) have shown an anti-  
449 correlation (0.46) of tropospheric ozone with monsoon index over the Indian region. The years  
450 2011, 2012, 2014, and 2015 are classified as weak monsoon years and relatively higher ozone is  
451 seen during these years, whereas for the years 2013, 2016, and 2017, strong monsoon is observed,  
452 and average yearly ozone was lesser during these years (Figure 6 bottom left). The relative  
453 difference of AIRS ozone with ozonesonde in the upper tropospheric region also shows an anti-  
454 correlation (Figure 6) of 0.17 with total column water vapor. Furthermore, the larger ozone  
455 differences between AIRS and ozonesonde are associated with the lower water vapor (Figure S6),  
456 which may be arising due to the influence of ozone-sensitive water vapor (WV) channels in mid-  
457 Infra-red regions. Further, in the middle troposphere (600-300 hPa), a secondary ozone peak in  
458 post-monsoon is observed, which is suggested to be influenced by the biomass burning (Figure  
459 S7) over northern India that seems to be missing in the AIRS ozone.

460

461 In the middle troposphere (600 - 300 hPa) and lower stratosphere (100 - 50 hPa), AIRS retrievals  
462 show higher differences with respect to ozonesondes, while a nominal difference is observed for  
463 the middle troposphere and middle stratosphere (Figure S6). Furthermore, a systematic increase in  
464 standard deviation is also seen with the altitude. The higher standard deviations in the upper  
465 tropospheric and stratospheric regions are mainly due to higher ozone variability associated with

466 stratosphere-troposphere exchange (STE) processes over the Himalayan region (Naja et al., 2016;  
467 Bhardwaj et al., 2018).

468

### 469 **3.3 Statistical Analysis of AIRS Ozone Profiles**

470 Error analysis of AIRS retrieved ozone over the Himalayan region is performed with spatio-  
471 temporal collocated ozonesonde observations as a reference. The methodology to calculate the  
472 root mean square error (RMSE), bias, and standard deviation (STD) is described in section 2.3.  
473  $W_2$  weighting statistics are utilized due to abrupt changes in atmospheric ozone with altitude. Here  
474 bias and STD between AIRS and ozonesonde are calculated at different RTA layers from surface  
475 to 10 hPa. Figure 7 shows the average variation of bias and STD at different RTA layers from  
476 surface to 10 hPa over this region. The mean biases between ozonesonde and MLS, a high vertical  
477 resolution satellite instrument, are also shown in figure 7. In general, higher positive biases (~65%)  
478 and STDs (~25%) in AIRS ozone retrieval are seen in the UTLS region, where MLS agrees well  
479 with ozonesonde. In the lower and middle troposphere, the AIRS ozone retrieval is negatively  
480 biased (0 - 25%), which increases gradually from the surface to higher altitudes (~ 350hPa). A  
481 negative bias was also seen in the stratosphere of about 15%. Similar to the biases, STDs are also  
482 smaller in the lower troposphere and stratosphere, with values of nearly 15%. The higher statistical  
483 errors in the upper troposphere and the lower stratospheric region could be due to lower ozone  
484 partial pressure and frequent stratospheric to tropospheric transport events over the Himalayas  
485 (Rawat et al., 2020, 2021), which introduces errors either after a mismatch of events in AIRS  
486 coarser vertical resolution or due to complex topography. Additionally, the AIRS tropopause  
487 frequency distribution shows less ability of AIRS to capture deep intrusion events (Figure 3).  
488 Further, AIRS trace gas retrieval largely depends on successful temperature retrieval and uses

489 temperature retrieval as an input parameter (Maddy and Barnett, 2008). Hence, temperature  
490 retrieval error could also propagate to ozone, and statistical error analysis of AIRS temperature  
491 shows relatively higher biases ( $\sim 2$  K) in the upper tropospheric region (Figure S8).

492

493 The statistical error analysis was more-or-less similar for both true and smoothed ozonesonde  
494 profiles. However, notable reduction in tropospheric bias and vertical shifts of errors were also  
495 observed after applying the averaging kernel matrix to the true ozonesonde throughout the profile.  
496 A shift of the error peak is seen from the lower stratosphere to the upper troposphere. This could  
497 be due to the higher sensitivity of AIRS retrieval in the lower stratosphere, which would have  
498 minimized the error at these particular altitudes. However, in the upper troposphere, higher  
499 contribution of a-priories, as well as other factors (i.e., STE), might have resulted in larger biases  
500 and errors.

501

502 The histogram of differences between AIRS and ozonesonde (AK) is also studied at various  
503 defined layers (Figure 8). AIRS mostly underestimated ozone with a mean bias of 2.37 ppbv, 9.29  
504 ppbv, and 39.8 ppbv in 800 - 600 hPa, 600 - 300 hPa, and 100 - 50 hPa layers, respectively, while  
505 in the upper troposphere (300 - 100 hPa) AIRS overestimated with a mean bias of 43.22 ppbv.  
506 Furthermore, distributions of differences are skewed toward the negative values in the lower  
507 stratosphere and towards positive values in the upper troposphere. A more symmetric distribution  
508 over the negative axis is observed in the middle and lower troposphere. We also studied the  
509 correlation profiles for different seasons (Figure 8, right panel). A strong correlation is seen in the  
510 lower and middle troposphere for spring and summer, while there is a poor correlation for winter  
511 and autumn. In the lower troposphere, a larger difference between AIRS and ozonesonde(AK) is

512 observed, particularly during summer, with a relatively higher correlation mostly due to the greater  
513 concurrence of AIRS a-priori with ozonesonde(AK). Whereas, in the upper troposphere (300 - 100  
514 hPa), a larger difference during winter and spring is primarily due to frequent subtropical  
515 dynamics, while a higher correlation during the winter is mainly contributed from the AIRS  
516 retrieval. Furthermore, analysis of the correlation coefficient between AIRS and ozonesonde over  
517 different regions shows a higher correlation in the middle stratosphere (0.95) and lower  
518 stratosphere (0.92), followed by upper troposphere (0.68), lower troposphere (0.62), and middle  
519 troposphere (0.47).

520

### 521 **3.4 Assessment of AIRS Retrieval Algorithm with IASI and CrIS Radiance**

522 The MetOp/IASI and Soumi-NPP/CrIS radiance-based ozone products are assessed using  
523 ozonesonde data over the central Himalayan region for one year (April 2014 to April 2015),  
524 utilizing a total of 32 soundings. Here, the IASI and CrIS based ozone retrievals are research  
525 products provided by NOAA, whose retrieval is based on the AIRS retrieval algorithm and follows  
526 a similar averaging kernels matrix (Nalli et al., 2017). For IASI, due to the 09:30 ascending nodes  
527 (morning overpass in India),  $\pm 6$  h loose temporal collocation is used. However, CrIS and AIRS  
528 follow the same collocation due to a similar noontime overpass. The IASI, CrIS, and AIRS sensors  
529 have 8461, 1305, and 2378 IR channels, respectively. Hence, analyzing their satellite ozone  
530 products further helps to assess the AIRS retrieval algorithm for different IR radiances and channel  
531 sets.

532

533 Figure 9a shows the seasonal ozone profiles obtained from three IR satellite sensors along with  
534 ozonesonde for one year period. All sensors showed more-or-less similar ozone peak altitude and

535 ozone gradient. The estimated ozone peak altitude for ozonesonde, AIRS, IASI, and CrIS are 11.35  
536 hPa, 10 hPa, 9.11 hPa, and 7.78 hPa, respectively. The estimated average ozone gradient in regions  
537 between tropopause to gradient peak are 231.5 ppbv/hPa, 199.0 ppbv/hPa, 193.2 ppbv/hPa, and  
538 199.1 ppbv/hPa for ozonesonde, AIRS, CrIS, and IASI, respectively.

539

540 Moreover, the higher ozone values during spring throughout the troposphere are captured well by  
541 all satellite sensors. Higher ozone during spring and winter in the UTLS region is observed well  
542 by AIRS and IASI, similar to ozonesonde but such features seem to be missing in CrIS ozone  
543 retrieval. At the same time, CrIS sensitivity looks relatively low, where the possible role of the  
544 number of channels can be seen. However, IASI and AIRS have effectively captured the ozone  
545 seasonal variability.

546

547 Figure 9b shows the weighted statistical error analysis of IASI, CrIS, and AIRS ozone retrieval  
548 with the true ozonesonde observations. Here, the difference in sensitivity of the two data sets is  
549 not accounted for as this section's primary aim is to assess the AIRS retrieved algorithm using  
550 different IR sensor radiances and channel sets. All three space-borne sensors overestimated UTLS  
551 ozone by more than 50%, however, in the stratosphere and lower troposphere, the bias was slightly  
552 lower, and it is somewhat underestimated. Similar to bias, the STDs were also higher in the UTLS  
553 region by more than 60%. A consistent larger differences in the UTLS region for all three IR  
554 satellite sensors that share the similar radiative transfer model and retrieval algorithm shows the  
555 possible influence of complex topography and the various STE processes, in introducing errors in  
556 retrieval processes, apart from input a-priories of the retrieval.

557



558 Additionally, Pearson correlations between ozonesonde and IASI, CrIS, and AIRS are also studied  
559 at five atmospheric layers (i.e., 600-800 hPa, 300-600 hPa, 100-300 hPa, 50-100 hPa, and 10 - 50  
560 hPa) (Table 2). A relatively stronger positive correlation is found in the middle stratosphere (50-  
561 100 hPa) and lower stratosphere (50 - 100 hPa), which was highest for AIRS, followed by CrIS  
562 and IASI, and a relatively low correlation is observed in the middle troposphere (300-600 hPa) for  
563 AIRS and IASI (~ 44% and 31%), while CrIS shows the poorest correlation in the lower  
564 troposphere about 9%. The lower concurrence between ozonesonde and the satellite sensors in the  
565 lower troposphere could be due to lower sensitivity and shorter lifetime of near-surface ozone that  
566 could increase the a-priori contribution and sampling mismatch, respectively.

567

### 568 **3.5 Columnar Ozone**

#### 569 **3.5.1 Total Column Ozone (TCO)**

570 Figure 10a shows variations in monthly average total column ozone (TCO) from ozonesonde,  
571 AIRS, and OMI during 2011 - 2017. Here the box plots are also overlaid on the mean column to  
572 describe the distribution of monthly column data. In general, the TCO is higher during spring,  
573 which subsequently drops in summer-monsoon. AIRS TCO shows a bimodal monthly variation  
574 which is not seen in the ozonesonde and OMI observations, otherwise, its monthly variation is in  
575 reasonable agreement with ozonesonde. The OMI TCO is in a good match with the ozonesonde  
576 with a maximum difference of up to about 5 DU. Table 3 shows the difference in the TCO between  
577 AIRS, OMI, and ozonesonde. AIRS shows considerable overestimation in the range of 2.2 - 22  
578 DU for some months while notable underestimation (1.8 - 4 DU) for others, with respect to both  
579 ozonesonde and OMI. The correlation between AIRS TCO and ozonesonde TCO is found to be  
580 0.5 (Table S4). To further understand the cause of bimodal variations in AIRS (higher ozone during

581 August, September, and October), the AIRS ozone profiles were integrated between different  
582 stratospheric regions (100 - 70 hPa, 70 - 50 hPa, 50 - 20 hPa, and 20 - 1 hPa) and we found that  
583 the elevated total ozone during post-monsoon is mainly contributed from the altitude above 50  
584 hPa.

585

### 586 **3.5.2 UTLS Ozone Column**

587 Figure 10b shows the variations in the monthly average UTLS ozone column for collocated and  
588 concurrent observations of AIRS, MLS, and ozonesonde during 2011 - 2017. The UTLS region  
589 extends between 400 hPa to 70 hPa (Bian et al., 2007) for ozonesonde and AIRS, while for MLS,  
590 the region between 261 hPa to 70 hPa is utilized. The recommended pressure levels for MLS v4  
591 ozone retrieval are above 261 hPa (Livesey et al., 2013; Schwartz et al., 2015). In contrast to TCO,  
592 higher ozone in UTLS is seen during the winter and spring (~ 45 DU) when there are recurring  
593 downward transport events, while a clear drop of the column during the summer-monsoon shows  
594 the convective transport of cleaner oceanic air to the higher altitudes. All the collocated  
595 observations are able to capture the monthly variation effectively. However, there is a substantial  
596 overestimation by more than 3 DU (Table S5) for all the months in AIRS measurements and MLS  
597 mostly underestimate it, except during winter due to smaller integrated columns. Furthermore, the  
598 larger whiskers of the box plot during winter and spring show the larger variations of the ozone in  
599 the UTLS region. Though there were notable overestimations compared to ozonesonde, still UTLS  
600 monthly variations are captured well by AIRS with a correlation of up to 75% (Table S4). In  
601 addition, the correlation of ozonesonde and AIRS ozone at each pressure level in the UTLS region  
602 is 0.81, which further increases with ozonesonde(AK) (of about 0.94). The persistent biases in the

603 satellite retrievals arises due to inadequate input parameters that can be improved by using more  
604 accurate initial parameters and surface emissivity (Dufour et al., 2012; Boynard et al., 2018).

605

606

### 607 **3.5.3 Tropospheric Ozone Column**

608 Figure 10c shows the variations in the monthly average tropospheric ozone column utilizing  
609 various collocated data sets during 2011 - 2017. The tropospheric ozone column is calculated by  
610 integrating ozone profiles from the surface to the tropopause. WMO-defined lapse rate calculation  
611 method is used to calculate tropopause height from balloon-borne and AIRS observations (Figure  
612 3). Higher tropospheric ozone is observed during the spring and early summer ( $> 45$  DU) when  
613 annual crop-residue burning (Figure S7) events occur over northern India, apart from downward  
614 transport from the stratosphere. A few cases of downward transport are discussed in the next  
615 section. The tropospheric ozone column drops rapidly during the summer-monsoon when pristine  
616 marine air reaches Nainital. A slight increase of column is also seen during the autumn, which is  
617 again influenced by post-monsoon crop residue burning practices (Figure S7) over northern India  
618 (Bhardwaj et al., 2016). The AIRS is able to capture the monthly variations very effectively;  
619 however, there are larger biases. The biases with ozonesonde are higher when the tropopause is  
620 taken from the balloon-borne observation, while with AIRS provided tropopause, the biases are  
621 lesser or mostly within the one sigma limit. The correlation between ozonesonde and AIRS, when  
622 used AIRS tropopause, is very strong (0.72). Like AIRS, the OMI/MLS column is in good  
623 agreement and able to produce monthly variations; however, there are larger differences during  
624 winter and spring of more than 10 DU. The tropospheric ozone column from ozonesonde is  
625 different for balloon-borne LRT and AIRS tropopause, which could be due to the lower vertical

626 resolution of AIRS. AIRS calculates tropopause with an uncertainty of 1-2 km (Divakarla et al.,  
627 2006). It can also be seen that on average a lower (about 28%) tropopause pressure (or higher  
628 altitude) is calculated by AIRS compare to ozonesonde measurements (Figure 3).

629

### 630 **3.6 Case Studies of Biomass Burning and Downward Transport**

631 Over northern India, extensive agriculture practices and forest fires influence ozone at the surface  
632 and higher altitudes (Kumar et al., 2011; Cristofanelli et al., 2014; Bhardwaj et al., 2016; Bhardwaj  
633 et al., 2018). Based on MODIS fire counts, the days in between 1 March to 15 April over northern  
634 India are classified as the low fire periods (LFP) as considered in previous studies over this region.  
635 The high fire period (HFP) is classified when the fire counts over the observational site are more  
636 than the median fire counts in the biomass burning period, typically from mid-April to May  
637 (Bhardwaj et al., 2016). A total of 32 soundings (mid-April to May) are classified as HFP and 33  
638 soundings (March to mid-April) are classified as LFP. Figure 11 (left) shows the average ozone  
639 profiles up to 6 km from ozonesonde and AIRS observations during HFP and LFP. The  
640 ozonesonde data show enhancement in ozone by about 5 ppbv to about 11 ppbv during HFP as  
641 compared to LFP that is accounting for a 5-20% increase. It is important to mention that  
642 enhancement is greater in higher altitude regions that drop gradually above 400 hPa. The  
643 enhancement is slightly lower (10-15%) in the AIRS profile, where most of it is contributed by the  
644 a-priori profile (Figure S8).

645

646 Deep stratospheric intrusion or the downward transport (DT) of ozone-rich air from the  
647 stratosphere to the troposphere significantly influences ozone profiles over the subtropical regions  
648 (Collins, et al., 2003; Zhu, et al., 2006; Lal et al., 2014). Over the subtropical Himalayas, such

649 ozone intrusions are observed during the winter and spring seasons (Zhu et al., 2006; Ojha et al.,  
650 2014). The DT events are classified based on the higher ozone in middle - upper troposphere seen  
651 from ozonesonde with relatively larger Ertel potential vorticity (EPV) and lower humidity in  
652 MERRA-2 reanalysis data. Based on this, 10 soundings (between January and mid-April) are  
653 classified as DT events for ozonesonde and AIRS. Figure 11 (right) shows ozone profiles from  
654 ozonesonde (AK) and AIRS observations for high ozone DT events as well as the average ozone  
655 profiles of corresponding months excluding the DT event. Though there are persistent positive  
656 biases in AIRS ozone profile compared to ozonesonde in the middle/upper troposphere, still both  
657 the observations have captured the influence of the downward transport on the ozone profile very  
658 effectively and show an increase in the ozone of 10 - 20% in altitude range 2 - 16 km. Ozonesonde  
659 based observations have shown about twofold increase in upper-middle tropospheric ozone due to  
660 downward ozone transport over this region (Ojha et al., 2014). Further, the first guess profile's  
661 contribution to AIRS retrieval during DTs is negligible (Figure S9) and shows the main  
662 contribution from the AIRS observations itself. So, despite the persistent biases in the AIRS and  
663 ozonesonde observations, AIRS is able to capture the influences of downward transport (DT) on  
664 ozone profile notably well.

665

### 666 **3.7 Ozone Radiative Forcing**

667 Radiative forcing is a valuable metric to estimate the radiative impacts of any anthropogenic or  
668 natural activity on the climate system (Ramaswamy et al., 2001). It measures the net radiation at  
669 the surface, tropopause, and the top of the atmosphere due to any atmospheric constituents. Here  
670 we discuss the ozone radiative forcing (RF) at the surface in the ultraviolet (UV) spectral range  
671 (Antón et al., 2014; Mateos et al., 2020) using the ozonesonde, OMI, and AIRS total column ozone

672 (TCO) data. The RF is calculated based on Antón et al. (2014), relative to 1979 utilizing TOMS  
673 TOC data in 1979, monthly averaged solar zenith angles of site, clearness index based on  
674 Chakraborty et al., (2014) and Hawas et al., (1984), and respective monthly average TCO data of  
675 AIRS, OMI, and ozonesonde. Rather than quantifying the RF values here, our primary focus is to  
676 show how the discrepancies of satellite ozone data (mainly AIRS) can impact the calculation of  
677 RF values. Figure 12 shows the seasonal average ozone radiative forcing (RF) relative to 1979.  
678 The annual average ozone RF during 2011 -2017 is 4.86, 4.04, and 2.96 mW/m<sup>2</sup> for ozonesonde,  
679 OMI, and AIRS, respectively. The RF values for ozonesonde and OMI are comparable to Mateos  
680 et al. (2020) (4 mW/m<sup>2</sup>) for the extratropical region. However, for AIRS, the RF value is lower by  
681 45%. Further, the seasonal average ozone RF (2011-2017) is consistent between ozonesonde and  
682 OMI, while notable differences are seen in AIRS except during the winter season when differences  
683 are marginal (Figure 12). Also from Table 3, it is clear that the higher total ozone bias during  
684 autumn (as high as 22 DU) contributes to higher RF differences in autumn (Figure 12).

685

#### 686 **4. Summary and Conclusions**

687 This study has utilized 242 ozone soundings (during 2011 - 2017) conducted over the Himalayan  
688 station (Nainital) to evaluate the AIRS version 6 ozone product and study the performance during  
689 biomass burning events, ozone downward transport events and estimation of ozone radiative  
690 forcing. AIRS ozone retrieval is evaluated in terms of retrieval sensitivity, retrieval biases, retrieval  
691 errors, and ability to retrieve the natural variability of columnar ozone at different altitude regions.  
692 This study is the first of its kind in the Himalayan region. The AIRS averaging kernels information  
693 was applied to ozonesonde for a like-for-like comparison to overcome their sensitivity differences.  
694 The monthly profile evaluation shows ozone peak and ozone altitude dependency is captured well

695 by AIRS retrieval with smaller but notable underestimation (5 - 20%) in the lower-middle  
696 troposphere and stratosphere, while overestimation in the UTLS region as high as 102%. We show  
697 the larger sensitivity of AIRS ozone for the summer monsoon in the UTLS region, where the biases  
698 between AIRS and ozonesonde improved remarkably after applying AIRS averaging kernel  
699 information.

700

701 The weighted statistical error analysis of AIRS retrieved ozone profiles shows higher positive  
702 biases (65%) and STD (25%) in the upper troposphere. In the lower and middle troposphere, AIRS  
703 ozone was negatively biased, apart from the stratosphere. In addition, though the biases and errors  
704 are higher in the upper troposphere, there is a larger correlation of about 81% showing the  
705 capability of AIRS to retrieve upper tropospheric ozone variability with certain positive biases that  
706 can be eliminated by choosing better emissivity inputs or other retrieval inputs. The AIRS ozone  
707 retrieval algorithm was further evaluated using the radiance of IASI and CrIS sensors; these  
708 sensors provided similar error statistics as seen for AIRS.

709

710 The AIRS-derived columnar ozone amounts (i.e., total, UTLS, and tropospheric ozone) are also  
711 evaluated to see whether the ozone variability at different altitude regions is being retrieved  
712 correctly. The UTLS and tropospheric ozone monthly variations are captured well by AIRS with  
713 persistent positive biases. However, the total ozone column shows bimodal monthly variations,  
714 which was not evident in the ozonesonde and OMI total ozone observations. Further, we found a  
715 higher total ozone column in AIRS during autumn, which is mostly coming from the stratospheric  
716 region above 50 hPa. The capabilities of AIRS to capture various biomass burning and downward

717 transport events have also been studied. AIRS captures all such events reasonably well with  
718 notable contributions of the a-priori, particularly in the biomass burning events.

719

720 Unlike the well-mixed greenhouse gases, the ozone radiative forcing (RF) remains uncertain due  
721 to inadequate budget estimates and complex chemical processes. The total ozone discrepancies of  
722 AIRS lead to show lower RF (by about 45%) and greater uncertainty in this Himalayan region.  
723 Stevenson et al. (2013) have shown that a few percent uncertainties in ozone concentrations can  
724 produce a spread of ~17% in ozone RF estimations. Here, the role of in-situ observations from  
725 ozone soundings is shown to be important in improving the satellite retrieved ozone over the  
726 Himalayan region by assessing and providing insights upon its error and bias. This information  
727 could be applied to the ozone retrieval from other satellite data sets, having long-term coverage.  
728 This will help in better understanding regional ozone and radiation budgets over this Himalayan  
729 region having complex topography.

730

### 731 **Acknowledgments**

732 We are grateful to Director ARIES and ISRO-ATCTM project for supporting this work. Help from  
733 Deepak and Nitin in balloon launches and coordination with the air traffic control is highly  
734 acknowledged. The National Center for Atmospheric Research is sponsored by the National  
735 Science Foundation. SL is grateful to INSA, New Delhi for the position and Director PRL,  
736 Ahmedabad for the support. We highly acknowledge NOAA and NASA-EARTHDATA online  
737 data portals for providing IASI, AIRS, and CrIS label2 data. We thank the NASA Goddard Space  
738 Flight Center Ozone Processing Team for providing the OMI/MLS tropospheric ozone, OMI total  
739 ozone column and JPL for MLS ozone profile. We would also like to acknowledge the use of the



740 MODIS fire data through FIRMS archive download. Use of map from Google earth is also  
741 acknowledged. We thank the reviewers for their constructive comments and valuable suggestions.

742

743

744 **Data availability:** Satellite data are available in the respective web portal. Ozonesonde data could  
745 be made available on a reasonable request by writing to the corresponding author.

746

#### 747 **References**

748 Antón, M., D. Mateos, R. Román, A. Valenzuela, L. Alados-Arboledas, and F. J. Olmo.: A method  
749 to determine the ozone radiative forcing in the ultra-violet range from experimental data, J.  
750 Geophys. Res. Atmos., 119, 1860–1873, doi:10.1002/2013JD020444, 2014.

751

752 Aghedo, A.M., Bowman, K.W., Worden, H.M., Kulawik, S.S., Shindell, D.T., Lamarque, J.F.,  
753 Faluvegi, G., Parrington, M., Jones, D.B.A. and Rast, S.: The vertical distribution of ozone  
754 instantaneous radiative forcing from satellite and chemistry climate models. Journal of  
755 Geophysical Research: Atmospheres, 116(D1), 2011.

756

757 Bai, W., Wu, C., Li, J. and Wang, W.: Impact of terrain altitude and cloud height on ozone remote  
758 sensing from satellite, Journal of Atmospheric and Oceanic Technology, 31(4), pp.903-912, 2014.

759

760 Barre, J., Peuch, V.H., Attié, J.L., Amraoui, L.E., Lahoz, W.A., Josse, B., Claeysman, M. and  
761 Nedelec, P.: Stratosphere-troposphere ozone exchange from high resolution MLS ozone analyses,  
762 Atmos. Chem. Phys., 12(14), pp.6129-6144, 2012.

763

764 Bhardwaj, P., Naja, M., Kumar, R. and Chandola, H.C.: Seasonal, interannual, and long-term  
765 variabilities in biomass burning activity over South Asia, *Environmental Science and Pollution*  
766 *Research*, 23(5), pp.4397-4410, 2016.

767

768 Bhardwaj, P., Naja, M., Rupakheti, M., Lupascu, A., Mues, A., Panday, A. K., Kumar, R., Mahata,  
769 K. S., Lal, S., Chandola, H. C., and Lawrence, M. G.: Variations in surface ozone and carbon  
770 monoxide in the Kathmandu Valley and surrounding broader regions during SusKat-ABC field  
771 campaign: role of local and regional sources, *Atmos. Chem. Phys.*, 18, 11949–11971,  
772 <https://doi.org/10.5194/acp-18-11949-2018>, 2018.

773

774 Bhartia, P.K., McPeters, R.D., Mateer, C.L., Flynn, L.E. and Wellemeyer, C.: Algorithm for the  
775 estimation of vertical ozone profiles from the backscattered ultraviolet technique, *J. Geophys. Res.*  
776 *Atmos.*, 101(D13), pp.18793-18806, 1996.

777

778 Bian, J., Gettelman, A., Chen, H. and Pan, L.L.: Validation of satellite ozone profile retrievals  
779 using Beijing ozonesonde data, *J. Geophys. Res. Atmos.*, 112(D6), 2007.

780

781 Boynard, A., Hurtmans, D., Koukouli, M.E., Goutail, F., Bureau, J., Safieddine, S., Lerot, C.,  
782 Hadji-Lazaro, J., Wespes, C., Pommereau, J.P. and Pazmino, A.: Seven years of IASI ozone  
783 retrievals from FORLI: validation with independent total column and vertical profile  
784 measurements, *Atmos. Meas. Tech.*, 9(9), pp.4327-4353, 2016.

785

786 Boynard, A., Hurtmans, D., Garane, K., Goutail, F., Hadji-Lazaro, J., Koukouli, M. E., Wespes,  
787 C., Vigouroux, C., Keppens, A., Pommereau, J.-P., Pazmino, A., Balis, D., Loyola, D., Valks, P.,  
788 Sussmann, R., Smale, D., Coheur, P.-F., and Clerbaux, C.: Validation of the IASI  
789 FORLI/EUMETSAT ozone products using satellite (GOME-2), ground-based (Brewer–Dobson,  
790 SAOZ, FTIR) and ozonesonde measurements, *Atmos. Meas. Tech.*, 11, 5125–5152,  
791 <https://doi.org/10.5194/amt-11-5125-2018>, 2018.

792

793 Chakraborty, S., Sadhu, P.K. and Nitai, P.A.L.: New location selection criterions for solar PV  
794 power plant. *International Journal of Renewable Energy Research*, 4(4), pp.1020-1030, 2014.

795

796 Clerbaux, C., Hadji-Lazaro, J., Turquety, S., George, M., Coheur, P.F., Hurtmans, D., Wespes, C.,  
797 Herbin, H., Blumstein, D., Tourniers, B. and Phulpin, T.: The IASI/MetOp1 Mission: First  
798 observations and highlights of its potential contribution to GMES2, *Space Research Today*, 168,  
799 pp.19-24, 2007.

800

801 Coheur, P.F., Barret, B., Turquety, S., Hurtmans, D., Hadji-Lazaro, J. and Clerbaux, C.: Retrieval  
802 and characterization of ozone vertical profiles from a thermal infrared nadir sounder, *J. Geophys.*  
803 *Res. Atmos.*, 110(D24), 2005.

804

805 Collins, W. J., R. G. Derwent, B. Garnier, C. E. Johnson, M. G. Sanderson, and D. S. Stevenson.:  
806 Effect of stratosphere-troposphere exchange on the future tropospheric ozone trend, *J. Geophys.*  
807 *Res.*, 108(D12), 8528, doi:10.1029/2002JD002617, 2003.

808

809 Cristofanelli, P., Putero, D., Adhikary, B., Landi, T.C., Marinoni, A., Duchi, R., Calzolari, F., Laj,  
810 P., Stocchi, P., Verza, G. and Vuillermoz, E.: Transport of short-lived climate forcers/pollutants  
811 (SLCF/P) to the Himalayas during the South Asian summer monsoon onset, *Environmental*  
812 *Research Letters*, 9(8), p.084005, 2014.

813

814 Divakarla, M., Barnet, C., Goldberg, M., Maddy, E., Wolf, W., Flynn, L., Xiong, X., Wei, J., Zhou,  
815 L. and Liu, X.: Validation of Atmospheric Infrared Sounder (AIRS) temperature, water vapor, and  
816 ozone retrievals with matched radiosonde and ozonesonde measurements and forecasts, In  
817 *Multispectral, Hyperspectral, and Ultraspectral Remote Sensing Technology, Techniques, and*  
818 *Applications*, International Society for Optics and Photonics, Vol. 6405, p. 640503, 2006.

819

820 Divakarla, M., Barnet, C., Goldberg, M., Maddy, E., Irion, F., Newchurch, M., Liu, X., Wolf, W.,  
821 Flynn, L., Labow, G. and Xiong, X.: Evaluation of Atmospheric Infrared Sounder ozone profiles  
822 and total ozone retrievals with matched ozonesonde measurements, ECMWF ozone data, and  
823 Ozone Monitoring Instrument retrievals, *J. Geophys. Res. Atmos.*, 113(D15), 2008.

824

825 Dufour, G., Eremenko, M., Griesfeller, A., Barret, B., LeFlochmoën, E., Clerbaux, C., Hadji-  
826 Lazaro, J., Coheur, P.F. and Hurtmans, D.: Validation of three different scientific ozone products  
827 retrieved from IASI spectra using ozonesondes, *Atmos. Meas. Tech.*, 5(3), pp.611-630, 2012.

828

829 Ebi, K.L. and McGregor, G., Climate change, tropospheric ozone and particulate matter, and health  
830 impacts, *Environmental health perspectives*, 116(11), pp.1449-1455, 2008.

831

832 Fadnavis, S., Dhomse, S., Ghude, S., Iyer, U., Buchunde, P., Sonbawne, S. and Raj, P.E.: Ozone  
833 trends in the vertical structure of Upper Troposphere and Lower stratosphere over the Indian  
834 monsoon region, *International Journal of Environmental Science and Technology*, 11(2), pp.529-  
835 542, 2014.

836

837 Finlayson-Pitts, B.J. and Pitts, J.N.: Tropospheric air pollution: ozone, airborne toxics, polycyclic  
838 aromatic hydrocarbons, and particles, *Science*, 276(5315), pp.1045-1051, 1997.

839

840 Fishbein, E., Farmer, C.B., Granger, S.L., Gregorich, D.T., Gunson, M.R., Hannon, S.E.,  
841 Hofstadter, M.D., Lee, S.Y., Leroy, S.S. and Strow, L.L.: Formulation and validation of simulated  
842 data for the Atmospheric Infrared Sounder (AIRS), *IEEE Transactions on Geoscience and Remote*  
843 *Sensing*, 41(2), pp.314-329, 2003.

844

845 Fishman, J., Ramanathan, V., Crutzen, P.J. and Liu, S.C.: Tropospheric ozone and climate, *Nature*,  
846 282(5741), pp.818-820, 1979.

847

848 Fishman, J., Minnis, P. and Reichle Jr, H.G.: Use of satellite data to study tropospheric ozone in  
849 the tropics, *J. Geophys. Res. Atmos.*, 91(D13), pp.14451-14465, 1986.

850

851 Fishman, J. and Larsen, J.C.: Distribution of total ozone and stratospheric ozone in the tropics:  
852 Implications for the distribution of tropospheric ozone, *J. Geophys. Res. Atmos.*, 92(D6), pp.6627-  
853 6634, 1987.

854

855 Foret, G., Eremenko, M., Cuesta, J., Sellitto, P., Barré, J., Gaubert, B., Coman, A., Dufour, G.,  
856 Liu, X., Joly, M. and Doche, C.: Ozone pollution: What can we see from space? A case study, J.  
857 Geophys. Res. Atmos., 119(13), pp.8476-8499, 2014.

858

859 Forster, P.M., Bodeker, G., Schofield, R., Solomon, S. and Thompson, D.: Effects of ozone cooling  
860 in the tropical lower stratosphere and upper troposphere, Geophysical Research Letters, 34(23),  
861 2007.

862

863 Fry, M.M., Naik, V., West, J.J., Schwarzkopf, M.D., Fiore, A.M., Collins, W.J., Dentener, F.J.,  
864 Shindell, D.T., Atherton, C., Bergmann, D. and Duncan, B.N.: The influence of ozone precursor  
865 emissions from four world regions on tropospheric composition and radiative climate forcing.  
866 Journal of Geophysical Research: Atmospheres, 117(D7), 2012.

867

868 Gauss, M., Myhre, G., Pitari, G., Prather, M.J., Isaksen, I.S.A., Berntsen, T.K., Brasseur, G.P.,  
869 Dentener, F.J., Derwent, R.G., Hauglustaine, D.A. and Horowitz, L.W.: Radiative forcing in the  
870 21st century due to ozone changes in the troposphere and the lower stratosphere, J. Geophys. Res.  
871 Atmos., 108(D9), 2003.

872

873 Hauglustaine, D.A. and Brasseur, G.P.: Evolution of tropospheric ozone under anthropogenic  
874 activities and associated radiative forcing of climate, J. Geophys. Res. Atmos., 106(D23),  
875 pp.32337-32360, 2001.

876

877 Hawas, M.M. and Muneer, T.; Study of diffuse and global radiation characteristics in  
878 India. *Energy Conversion and Management*, 24(2), pp.143-149, 1984.

879

880 Hudson, R.D. and Thompson, A.M.: Tropical tropospheric ozone from total ozone mapping  
881 spectrometer by a modified residual method, *J. Geophys. Res. Atmos.*, 103(D17), pp.22129-  
882 22145, 1998.

883

884 Hegglin, M. I., Fahey, D. W., McFarland, M., Montzka, S. A., and Nash, E. R.: Twenty questions  
885 and answers about the ozone layer: 2014 update, *Scientific Assessment of Ozone Depletion: 2014*,  
886 84 pp., World Meteorological Organization, Geneva, Switzerland, ISBN 978-9966-076-02-1,  
887 2015.

888

889 Irion, F.W., Kahn, B.H., Schreier, M.M., Fetzer, E.J., Fishbein, E., Fu, D., Kalmus, P., Wilson,  
890 R.C., Wong, S. and Yue, Q.: Single-footprint retrievals of temperature, water vapor and cloud  
891 properties from AIRS. *Atmospheric Measurement Techniques*, 11(2), pp.971-995, 2018.

892

893 Kim, J.H. and Newchurch, M.J.: Climatology and trends of tropospheric ozone over the eastern  
894 Pacific Ocean: The influences of biomass burning and tropospheric dynamics, *Geophysical*  
895 *research letters*, 23(25), pp.3723-3726, 1996.

896

897 Komhyr, W.D., Barnes, R.A., Brothers, G.B., Lathrop, J.A. and Opperman, D.P.: Electrochemical  
898 concentration cell ozonesonde performance evaluation during STOIC 1989, *J. Geophys. Res.*  
899 *Atmos.*, 100(D5), pp.9231-9244, 1995.

900

901 Komhyr, W.D.: Nonreactive gas sampling pump. *Review of Scientific Instruments*, 38(7), pp.981-  
902 983, 1967.

903

904 Kumar, R., Naja, M., Satheesh, S.K., Ojha, N., Joshi, H., Sarangi, T., Pant, P., Dumka, U.C.,  
905 Hegde, P. and Venkataramani, S.: Influences of the springtime northern Indian biomass burning  
906 over the central Himalayas. *Journal of Geophysical Research: Atmospheres*, 116(D19), 2011.

907

908 Kumar, R., Naja, M., Pfister, G.G., Barth, M.C. and Brasseur, G.P.: Simulations over South Asia  
909 using the Weather Research and Forecasting model with Chemistry (WRF-Chem): set-up and  
910 meteorological evaluation, *Geoscientific Model Development*, 5(2), pp.321-343, 2012a.

911

912 Kumar, R., Naja, M., Pfister, G.G., Barth, M.C., Wiedinmyer, C. and Brasseur, G.P.: Simulations  
913 over South Asia using the Weather Research and Forecasting model with Chemistry (WRF-  
914 Chem): chemistry evaluation and initial results, *Geoscientific Model Development*, 5(3), pp.619-  
915 648, 2012b.

916

917 Lacis, A.A., Wuebbles, D.J. and Logan, J.A.: Radiative forcing of climate by changes in the  
918 vertical distribution of ozone, *J. Geophys. Res. Atmos.*, 95(D7), pp.9971-9981, 1990.

919

920 Lal S., S. Venkataramani, S. Srivastava, S. Gupta, M. Naja, T. Sarangi, X. Liu.: Transport effects  
921 on the vertical distribution of tropospheric ozone over the tropical marine regions surrounding  
922 India, *J. Geophys. Res.*, 118, 1513-1524, doi:10.1002/jgrd.50180, 2013.



923

924 Lal S., S. Venkataramani, N. Chandra, O. R. Cooper, J. Brioude, and M. Naja, Transport effects  
925 on the vertical distribution of tropospheric ozone over western India, *J. Geophys. Res. Atmos.*,  
926 119, doi:10.1002/2014JD021854, 2014.

927

928 Lal, S., Venkataramani, S., Naja, M., Kuniyal, J.C., Mandal, T.K., Bhuyan, P.K., Kumari, K.M.,  
929 Tripathi, S.N., Sarkar, U., Das, T. and Swamy, Y.V.: Loss of crop yields in India due to surface  
930 ozone: An estimation based on a network of observations, *Environmental Science and Pollution*  
931 *Research*, 24(26), pp.20972-20981, 2017.

932

933 Lawrence, M.G. and Lelieveld, J.: Atmospheric pollutant outflow from southern Asia: a review,  
934 *Atmospheric Chemistry and Physics*, 10(22), pp.11017-11096, 2010.

935

936 Lelieveld, J., Haines, A. and Pozzer, A.: Age-dependent health risk from ambient air pollution: a  
937 modelling and data analysis of childhood mortality in middle-income and low-income countries,  
938 *The lancet Planetary health*, 2(7), pp.e292-e300, 2018.

939

940 Livesey, N.J., Logan, J.A., Santee, M.L., Waters, J.W., Doherty, R.M., Read, W.G., Froidevaux,  
941 L. and Jiang, J.H.; Interrelated variations of O<sub>3</sub>, CO and deep convection in the  
942 tropical/subtropical upper troposphere observed by the Aura Microwave Limb Sounder (MLS)  
943 during 2004–2011. *Atmospheric Chemistry and Physics*, 13(2), pp.579-598, 2013.

944

945 Logan, J.A.: Tropospheric ozone: Seasonal behavior, trends, and anthropogenic influence, J.  
946 Geophys. Res. Atmos., 90(D6), pp.10463-10482, 1985.

947

948 Lu, X., Zhang, L., Liu, X., Gao, M., Zhao, Y. and Shao, J., 2018. Lower tropospheric ozone over  
949 India and its linkage to the South Asian monsoon. Atmospheric Chemistry and Physics, 18(5),  
950 pp.3101-3118.

951

952 Maddy, E.S. and Barnett, C.D.: Vertical resolution estimates in version 5 of AIRS operational  
953 retrievals, IEEE Transactions on Geoscience and Remote Sensing, 46(8), pp.2375-2384, 2008.

954

955 Mateos, D. and Antón, M.: Worldwide Evaluation of Ozone Radiative Forcing in the UV-B Range  
956 between 1979 and 2014. Remote Sensing, 12(3), p.436, 2020.

957

958 McPeters, R.D., Miles, T., Flynn, L.E., Wellemeyer, C.G. and Zawodny, J.M.: Comparison of  
959 SBUV and SAGE II ozone profiles: Implications for ozone trends, J. Geophys. Res. Atmos.,  
960 99(D10), pp.20513-20524, 1994.

961

962 McPeters, R.D., Labow, G.J. and Johnson, B.J.: A satellite-derived ozone climatology for  
963 balloonsonde estimation of total column ozone, J. Geophys. Res. Atmos., 102(D7), pp.8875-8885,  
964 1997.

965

966 McPeters, R.D., Labow, G.J. and Logan, J.A.: Ozone climatological profiles for satellite retrieval  
967 algorithms, J. Geophys. Res. Atmos., 112(D5), 2007.

968

969 Monahan, K.P., Pan, L.L., McDonald, A.J., Bodeker, G.E., Wei, J., George, S.E., Barnett, C.D. and  
970 Maddy, E.: Validation of AIRS v4 ozone profiles in the UTLS using ozonesondes from Lauder,  
971 NZ and Boulder, USA, *J. Geophys. Res. Atmos.*, 112(D17), 2007.

972

973 Monks, P.S., Archibald, A.T., Colette, A., Cooper, O., Coyle, M., Derwent, R., Fowler, D.,  
974 Granier, C., Law, K.S., Mills, G.E. and Stevenson, D.S.: Tropospheric ozone and its precursors  
975 from the urban to the global scale from air quality to short-lived climate forcer. *Atmospheric*  
976 *Chemistry and Physics*, 15(15), pp.8889-8973, 2015.

977

978 Munro, R., Siddans, R., Reburn, W.J. and Kerridge, B. J.: Direct measurement of tropospheric  
979 ozone distributions from space, *Nature*, 392(6672), pp.168-171, 1998.

980

981 Myhre, G., Aas, W., Cherian, R., Collins, W., Faluvegi, G., Flanner, M., Forster, P., Hodnebrog,  
982 Ø., Klimont, Z., Lund, M.T. and Mülmenstädt, J.: Multi-model simulations of aerosol and ozone  
983 radiative forcing due to anthropogenic emission changes during the period 1990–2015.  
984 *Atmospheric Chemistry and Physics*, 17(4), pp.2709-2720, 2017.

985

986 Naja, M., C Mallik, T. Sarangi, V Sheel, S. Lal, SO<sub>2</sub> measurements at a high altitude site in the  
987 central Himalayas: Role of regional transport, *Atmospheric Environment*,  
988 doi:10.1016/j.atmosenv.2014.08.031, 2014.

989

990 Naja M., Piyush Bhardwaj, N. Singh, Phani Kumar, R. Kumar, N. Ojha, Ram Sagar, S. K.  
991 Satheesh, K. Krishna Moorthy and V. R. Kotamarthi: High-frequency vertical profiling of

992 meteorological parameters using AMF1 facility during RAWEX–GVAX at ARIES, Nainital,  
993 Current Science, vol 111, issue 1, 2016.  
994  
995 Nalli, N.R., Barnet, C.D., Reale, A., Tobin, D., Gambacorta, A., Maddy, E.S., Joseph, E., Sun, B.,  
996 Borg, L., Mollner, A.K. and Morris, V.R.: Validation of satellite sounder environmental data  
997 records: Application to the Cross-track Infrared Microwave Sounder Suite, J. Geophys. Res.  
998 Atmos., 118(24), pp.13-628, 2013.  
999  
1000 Nalli, N.R., Gambacorta, A., Liu, Q., Tan, C., Iturbide-Sanchez, F., Barnet, C.D., Joseph, E.,  
1001 Morris, V.R., Oyola, M. and Smith, J.W.: Validation of Atmospheric Profile Retrievals from the  
1002 SNPP NOAA-Unique Combined Atmospheric Processing System. Part 2: Ozone, IEEE  
1003 Transactions on Geoscience and Remote Sensing, 56(1), pp.598-607, 2017.  
1004  
1005 Nassar, R., Logan, J.A., Worden, H.M., Megretskaia, I.A., Bowman, K.W., Osterman, G.B.,  
1006 Thompson, A.M., Tarasick, D.W., Austin, S., Claude, H. and Dubey, M.K. Validation of  
1007 Tropospheric Emission Spectrometer (TES) nadir ozone profiles using ozonesonde measurements.  
1008 Journal of Geophysical Research: Atmospheres, 113(D15), 2008.  
1009  
1010 Ojha, N., Naja, M., Sarangi, T., Kumar, R., Bhardwaj, P., Lal, S., Venkataramani, S., Sagar, R.,  
1011 Kumar, A. and Chandola, H.C.: On the processes influencing the vertical distribution of ozone  
1012 over the central Himalayas: Analysis of yearlong ozonesonde observations, Atmospheric  
1013 Environment, 88, pp.201-211, 2014.  
1014

1015 Pagano, T.S., Aumann, H.H., Hagan, D.E. and Overoye, K.: Prelaunch and in-flight radiometric  
1016 calibration of the Atmospheric Infrared Sounder (AIRS), IEEE transactions on geoscience and  
1017 remote sensing, 41(2), pp.265-273, 2003.

1018

1019 Pierce, R.B., Al-Saadi, J., Kittaka, C., Schaack, T., Lenzen, A., Bowman, K., Szykman, J., Soja,  
1020 A., Ryerson, T., Thompson, A.M. and Bhartia, P.: Impacts of background ozone production on  
1021 Houston and Dallas, Texas, air quality during the Second Texas Air Quality Study field mission,  
1022 J. Geophys. Res. Atmos., 114(D7), 2009.

1023

1024 Pittman, J.V., Pan, L.L., Wei, J.C., Irion, F.W., Liu, X., Maddy, E.S., Barnet, C.D., Chance, K.  
1025 and Gao, R.S.: Evaluation of AIRS, IASI, and OMI ozone profile retrievals in the extratropical  
1026 tropopause region using in situ aircraft measurements, J. Geophys. Res. Atmos., 114(D24), 2009.

1027

1028 Ramaswamy, V., Boucher, O., Haigh, J., Hauglustaine, D., Haywood, J., Myhre, G., Nakajima,  
1029 T., Shi, G.Y. and Solomon, S.: Radiative forcing of climate change. Climate change 2001: the  
1030 scientific basis. Contribution of working group I to the third assessment report of the  
1031 intergovernmental panel on climate change. DJ Griggs, M Noguier, PJ van der Linden, X Dai, K  
1032 Maskell and CA Johnson (Cambridge: Cambridge University Press) pp, 350, p.416, 2001.

1033

1034 Rawat, P., Naja, M., Thapliyal, P.K., Srivastava, S., Bhardwaj, P., Kumar, R., Bhattacharjee, S.,  
1035 Venkatramani, S., Tiwari, S.N. and Lal, S.: Assessment of vertical ozone profiles from INSAT-  
1036 3D sounder over the Central Himalaya. Current Science, 119(7), p.1113, 2020.

1037 Rawat, P. and Naja, M.: Remote sensing study of ozone, NO<sub>2</sub>, and CO: some contrary effects of  
1038 SARS-CoV-2 lockdown over India. *Environ Sci Pollut Res*, [https://doi.org/10.1007/s11356-021-](https://doi.org/10.1007/s11356-021-17441-2)  
1039 [17441-2](https://doi.org/10.1007/s11356-021-17441-2), 2021.

1040 Rodgers, C.D., 1976. Retrieval of atmospheric temperature and composition from remote  
1041 measurements of thermal radiation. *Reviews of Geophysics*, 14(4), pp.609-624.

1042

1043 Rodgers, C.D., 1990. Characterization and error analysis of profiles retrieved from remote  
1044 sounding measurements. *Journal of Geophysical Research: Atmospheres*, 95(D5), pp.5587-5595.

1045

1046 Rodgers, C.D. and Connor, B.J., 2003. Intercomparison of remote sounding instruments. *Journal*  
1047 *of Geophysical Research: Atmospheres*, 108(D3).

1048

1049 Sarangi T., M. Naja, N. Ojha, R. Kumar, S. Lal, S. Venkataramani, A. Kumar, R. Sagar and H. C.  
1050 Chandola: First simultaneous measurements of ozone, CO and NO<sub>y</sub> at a high altitude regional  
1051 representative site in the central Himalayas, *J. Geophys. Res.*, 119, doi:10.1002/2013JD020631,  
1052 2014.

1053

1054 Schwartz, M., Froidevaux, L., Livesey, N. and Read, W.: MLS/Aura Level 2 Ozone (O<sub>3</sub>) Mixing  
1055 Ratio V004, Greenbelt, MD, USA, Goddard Earth Sciences Data and Information Services Center  
1056 (GES DISC), 10.5067/Aura/MLS/DATA2017, 2015.

1057

1058 Shindell, D., Kuylenstierna, J.C., Vignati, E., van Dingenen, R., Amann, M., Klimont, Z.,  
1059 Anenberg, S.C., Muller, N., Janssens-Maenhout, G., Raes, F. and Schwartz, J.: Simultaneously

1060 mitigating near-term climate change and improving human health and food security, *Science*,  
1061 335(6065), pp.183-189, 2012.

1062

1063 Smit, H.G., Straeter, W., Johnson, B.J., Oltmans, S.J., Davies, J., Tarasick, D.W., Hoegger, B.,  
1064 Stubi, R., Schmidlin, F.J., Northam, T. and Thompson, A.M.: Assessment of the performance of  
1065 ECC-ozonesondes under quasi-flight conditions in the environmental simulation chamber:  
1066 Insights from the Juelich Ozone Sonde Intercomparison Experiment (JOSIE), *Journal of*  
1067 *Geophysical Research: Atmospheres*, 112(D19), 2007.

1068

1069 Srivastava S., Manish Naja, V. Thouret: Influences of regional pollution and long range transport  
1070 over Hyderabad using ozone data from MOZAIC, *Atmospheric Environment*, 117, pp.135-146,  
1071 2015.

1072

1073 Stevenson, D.S., Young, P.J., Naik, V., Lamarque, J.F., Shindell, D.T., Voulgarakis, A., Skeie,  
1074 R.B., Dalsoren, S.B., Myhre, G., Berntsen, T.K. and Folberth, G.A.: Tropospheric ozone changes,  
1075 radiative forcing and attribution to emissions in the Atmospheric Chemistry and Climate Model  
1076 Intercomparison Project (ACCMIP), *Atmos. Chem. Phys.*, 13(6), pp.3063-3085, 2013.

1077

1078 Susskind, J., Barnet, C.D. and Blaisdell, J.M.: Retrieval of atmospheric and surface parameters  
1079 from AIRS/AMSU/HSB data in the presence of clouds, *IEEE Transactions on Geoscience and*  
1080 *Remote Sensing*, 41(2), pp.390-409, 2003.

1081

1082 Susskind, J., Barnet, C., Blaisdell, J., Iredell, L., Keita, F., Kouvaris, L., Molnar, G. and Chahine,  
1083 M.: Accuracy of geophysical parameters derived from Atmospheric Infrared Sounder/Advanced  
1084 Microwave Sounding Unit as a function of fractional cloud cover, *J. Geophys. Res. Atmos.*,  
1085 111(D9), 2006.

1086  
1087 Tarasick, D., Galbally, I.E., Cooper, O.R., Schultz, M.G., Ancellet, G., Leblanc, T., Wallington,  
1088 T.J., Ziemke, J., Liu, X., Steinbacher, M. and Staehelin, J.: Tropospheric Ozone Assessment  
1089 Report: Tropospheric ozone from 1877 to 2016, observed levels, trends and uncertainties.  
1090 *Elementa: Science of the Anthropocene*, 7, 2019.

1091  
1092 Thornhill, G.D., Collins, W.J., Kramer, R.J., Olivié, D., Skeie, R.B., O'Connor, F.M., Abraham,  
1093 N.L., Checa-Garcia, R., Bauer, S.E., Deushi, M. and Emmons, L.K.: Effective radiative forcing  
1094 from emissions of reactive gases and aerosols—a multi-model comparison. *Atmospheric Chemistry  
1095 and Physics*, 21(2), pp.853-874, 2021.

1096  
1097 Veefkind, J.P., de Haan, J.F., Brinksma, E.J., Kroon, M. and Levelt, P.F.: Total ozone from the  
1098 Ozone Monitoring Instrument (OMI) using the DOAS technique, *IEEE transactions on geoscience  
1099 and remote sensing*, 44(5), pp.1239-1244, 2006.

1100  
1101 Verstraeten, W. W., Boersma, K. F., Zörner, J., Allaart, M. A. F., Bowman, K. W., and Worden,  
1102 J. R.: Validation of six years of TES tropospheric ozone retrievals with ozonesonde measurements:  
1103 implications for spatial patterns and temporal stability in the bias, *Atmos. Meas. Tech.*, 6, 1413–  
1104 1423, <https://doi.org/10.5194/amt-6-1413-2013>, 2013.

1105



1106 Wang, W.C., Zhuang, Y.C. and Bojkov, R.D.: Climate implications of observed changes in ozone  
1107 vertical distributions at middle and high latitudes of the Northern Hemisphere, *Geophysical*  
1108 *research letters*, 20(15), pp.1567-1570, 1993.

1109  
1110 Wang, B., R. Wu, K.-M. Lau: Interannual variability of Asian summer monsoon: Contrast between  
1111 the Indian and western North Pacific-East Asian monsoons. *J. Climate*, 14, 4073-4090, 2001.

1112  
1113 Wang, H.R., Damadeo, R., Flittner, D., Kramarova, N., Taha, G., Davis, S., Thompson, A.M.,  
1114 Strahan, S., Wang, Y., Froidevaux, L. and Degenstein, D.: Validation of SAGE III/ISS Solar  
1115 Occultation Ozone Products With Correlative Satellite and Ground-Based Measurements. *Journal*  
1116 *of Geophysical Research: Atmospheres*, 125(11), p.e2020JD032430, 2020.

1117  
1118 Wang, W., Cheng, T., van der A, R.J., de Laat, J. and Williams, J.E.: Verification of the  
1119 Atmospheric Infrared Sounder (AIRS) and the Microwave Limb Sounder (MLS) ozone algorithms  
1120 based on retrieved daytime and night-time ozone, *Atmos. Meas. Tech.*, 14(2), pp.1673-1687, 2021.

1121  
1122 Zhang, L., Jacob, D.J., Liu, X., Logan, J.A., Chance, K., Eldering, A. and Bojkov, B.R.:  
1123 Intercomparison methods for satellite measurements of atmospheric composition: application to  
1124 tropospheric ozone from TES and OMI. *Atmospheric Chemistry and Physics*, 10(10), pp.4725-  
1125 4739, 2010.

1126

1127 Zhu, T., W. Lin, Y. Song, X. Cai, H. Zou, L. Kang, L. Zhou, and H. Akimoto: Downward transport  
1128 of ozone-rich air near Mt. Everest, *Geophys. Res. Lett.*, 33, L23809, doi:10.1029/2006GL027726,  
1129 2006.

1130  
1131 Ziemke, J.R., Chandra, S. and Bhartia, P. K.: Two new methods for deriving tropospheric column  
1132 ozone from TOMS measurements: Assimilated UARS MLS/HALOE and convective-cloud  
1133 differential techniques, *J. Geophys. Res. Atmos.*, 103(D17), pp.22115-22127, 1998.

1134  
1135 Ziemke, J.R., Chandra, S., Duncan, B.N., Froidevaux, L., Bhartia, P.K., Levelt, P.F. and Waters,  
1136 J.W.: Tropospheric ozone determined from Aura OMI and MLS: Evaluation of measurements and  
1137 comparison with the Global Modeling Initiative's Chemical Transport Model, *J. Geophys. Res.*  
1138 *Atmos.*, 111(D19), 2006.

1139  
1140 Zhang, R., Wang, H., Qian, Y., Rasch, P.J., Easter, R.C., Ma, P.L., Singh, B., Huang, J. and Fu,  
1141 Q.: Quantifying sources, transport, deposition, and radiative forcing of black carbon over the  
1142 Himalayas and Tibetan Plateau. *Atmospheric Chemistry and Physics*, 15(11), pp.6205-6223, 2015.

1143  
1144  
1145  
1146  
1147  
1148  
1149

1150 **Table 1.** The mean values and corresponding standard errors of ozone mixing ratio (ppbv) from  
 1151 ozonesonde, ozonesonde(AK) and AIRS over Nainital at six pressure levels and during winter,  
 1152 spring, summer-monsoon, autumn are given. The number of ozonesonde flights during four  
 1153 seasons are mentioned in the bracket.

Pressure levels		706 (hPa)	496 (hPa)	300 (hPa)	103 (hPa)	29 (hPa)	14.4 (hPa)
Winter (61)	ozonesonde	55.1±0.9	54.4±0.7	69.5±2.8	238.8±15.0	4569.3±67.8	7620.6±140.1
	ozonesonde (AK)	48.6±0.4	55.9±0.6	70.4±1.8	187.3±3.6	5249.1±78.8	8214.9±105.7
	AIRS	46.5±0.3	52.2±0.6	68.7±1.2	354.4±8.4	4428.2±55.8	6616.4±56.0
Spring (72)	ozonesonde	71.6±1.8	70.2±1.5	81.5±2.8	223.9±12.7	4747.0±42.6	8242.3±101.6
	ozonesonde (AK)	58.7±0.7	69.1±1.1	80.3±1.4	221.8±3.6	5137.8±63.4	8784.4±96.6
	AIRS	55.3±0.4	60.7±0.7	78.6±1.0	389.2±6.0	4687.4±38.2	7852.4±97.0
Summer- monsoon (55)	ozonesonde	53.0±2.7	65.1±2.7	82.1±2.5	138.6±3.4	4642.9±26.4	8493.6±91.1
	ozonesonde (AK)	44.1±1.2	62.3±1.7	68.7±1.7	224.3±3.4	5271.3±44.6	9233.8±72.4
	AIRS	48.8±0.5	57.5±0.5	63.6±0.6	267.4±5.5	4710.0±48.2	8333.1±82.5
Autumn (54)	ozonesonde	53.0±1.1	63.8±1.6	72.7±1.6	144.6±6.2	4439.3±28.2	8613.7±77.5
	ozonesonde (AK)	50.4±0.5	61.0±0.8	64.1±0.9	169.0±2.0	5086.3±38.7	9035.8±80.7
	AIRS	46.0±0.3	51.3±0.4	56.9±30.5	241.8±3.6	4635.4±43.9	7984.9±97.6

1154 **Table 2.** Coefficient of determination ( $r^2$ ) of three IR satellite sensors (AIRS, IASI and CrIS) ozone  
 1155 retrieval in five broad layers with respect to ozonesonde observations.

	Coefficient of determination ( $r^2$ )		
	AIRS	IASI	CrIS
600 - 800 hPa	0.52	0.34	0.09
300 - 600 hPa	0.44	0.31	0.22
100 - 300 hPa	0.45	0.44	0.45
50-100 hPa	0.87	0.76	0.82
10 - 50 hPa	0.94	0.80	0.94

1156

1157

1158 **Table 3.** Total column ozone (TCO) differences in DU between AIRS, OMI and ozonesonde,  
 1159 during twelve months.

TCO Diff. (DU)	Jan	Feb	Mar	Apr	May	Jun	Jul	Aug	Sep	Oct	Nov	Dec
AIRS-OMI	-3.9	2.2	-1.8	13.2	16.7	18	-2.2	17.2	22.1	13.2	0.0	-2.7
AIRS-ozonesonde	-2.1	3.5	6.0	8.1	19.4	11.8	-2.3	22.3	21.6	15.0	5.6	5.2

1160

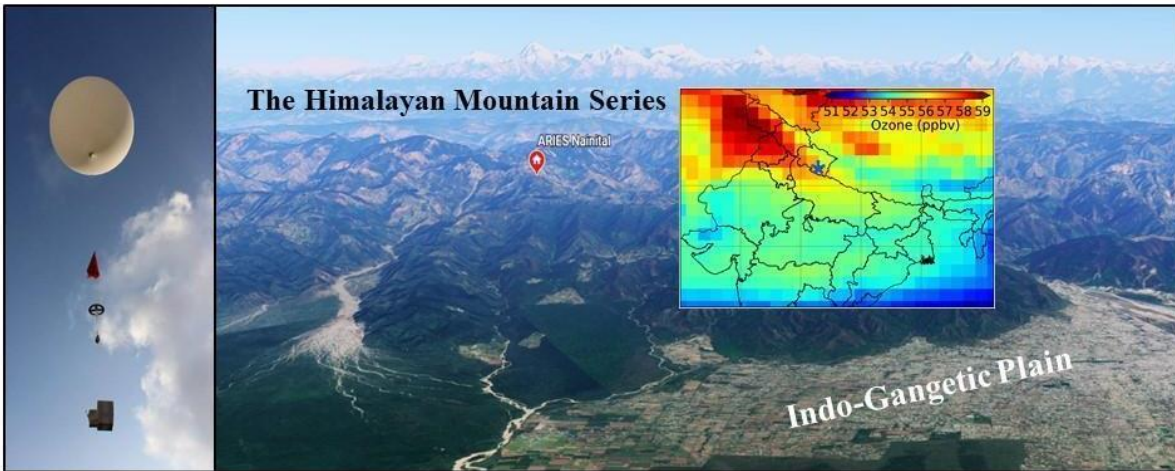
1161

1162

1163

1164

1165



1166

1167 **Figure 1.** Location (red color circle) of the balloon launching site (Map from Google Earth, 2021)  
1168 situated in the Aryabhata Research Institute of Observational Sciences (ARIES) (29.4° N, 79.5°  
1169 E, and 1793 m elevation), Nainital in the central Himalaya. The spatial distribution of ozone  
1170 (AIRS) at 500 hPa is also shown over northern India and the location of the site is marked with a  
1171 blue star. A photo of balloon, together with parachute, unwinder, ozonesonde along with GPS-  
1172 radiosonde above the observation site is also shown at the left.

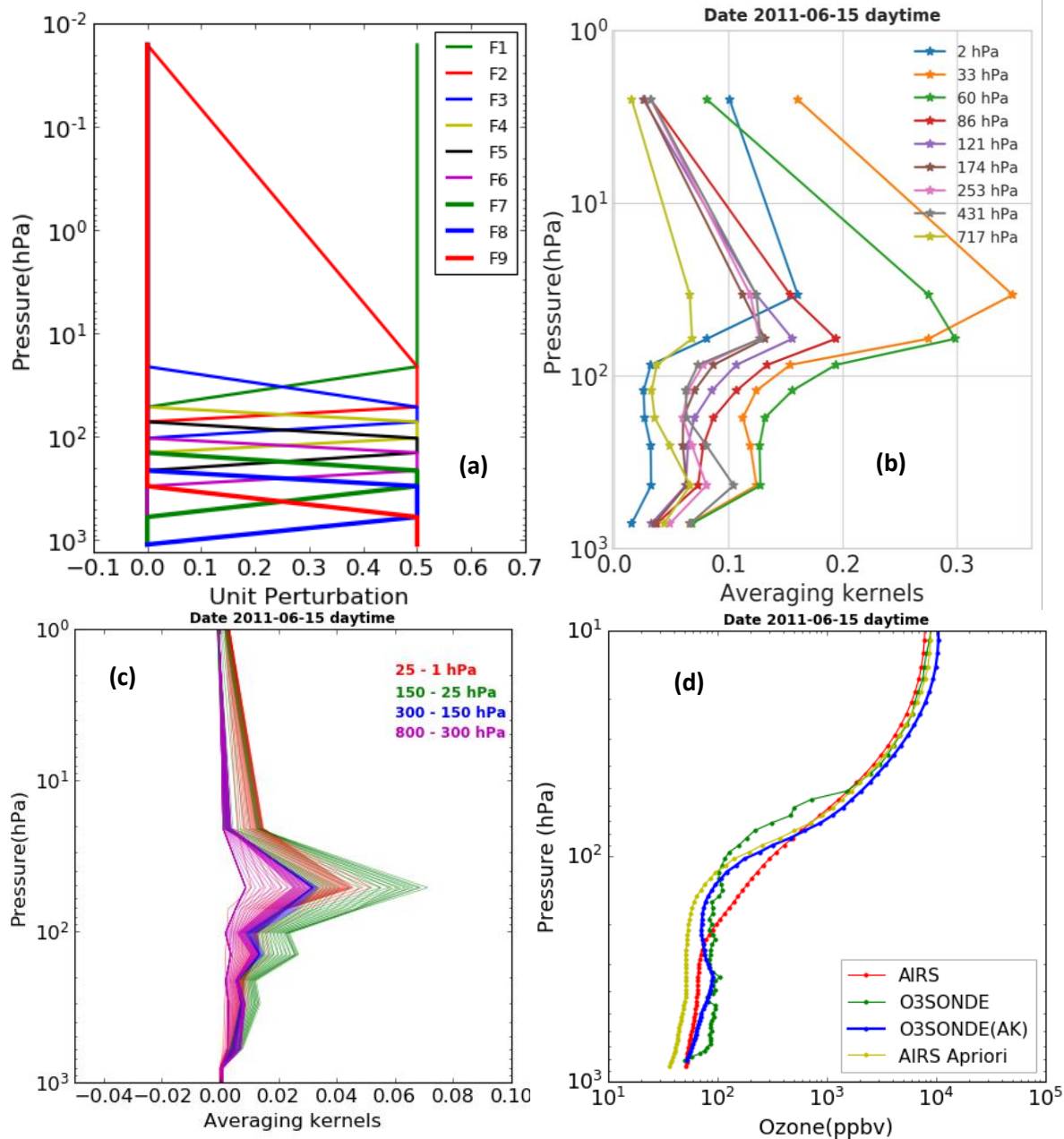
1173

1174

1175

1176

1177

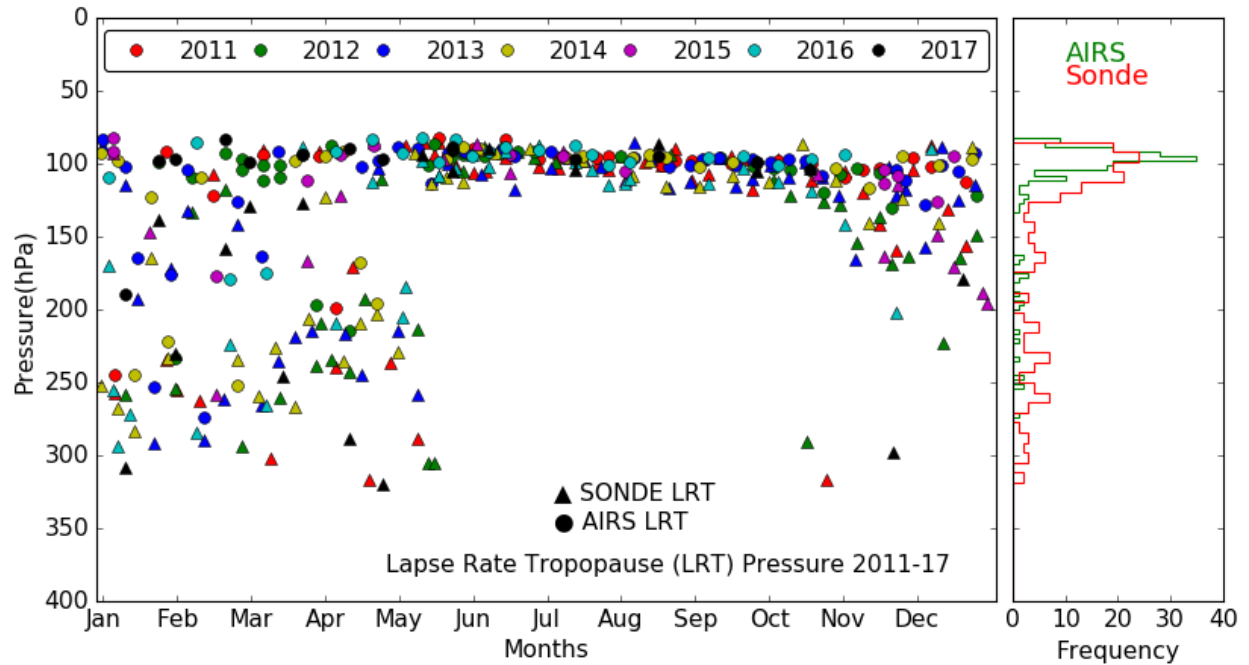


1178

1179

1180

1181 **Figure 2.** (a) Nine trapezoid functions used for ozone retrieval in AIRS-V6. (b) AIRS ozone  
 1182 averaging kernel matrix over Nainital at 9 levels vertical grid. (c) Calculated AIRS averaging  
 1183 kernel matrices at 100 RTA grids after applying the trapezoid function. (d) An example of ozone  
 1184 profiles using different data sets for 15 Jun 2011 over the observation site.



1185

1186 **Figure 3.** Lapse rate tropopause pressure monthly variation from balloon-borne and AIRS  
 1187 observations and respective frequency distributions during 2011 - 2017.

1188

1189

1190

1191

1192

1193

1194

1195

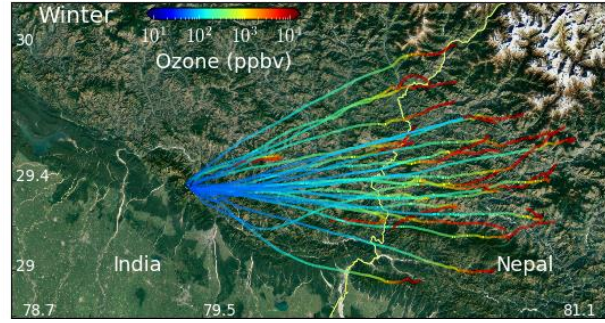
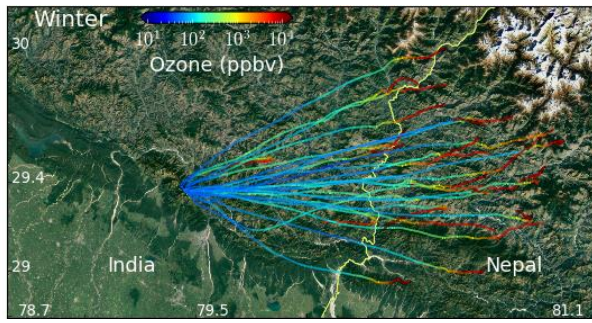
1196

1197

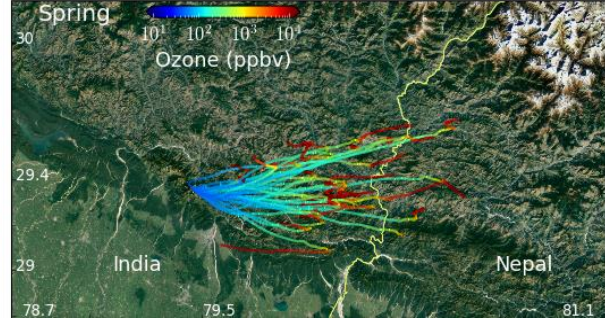
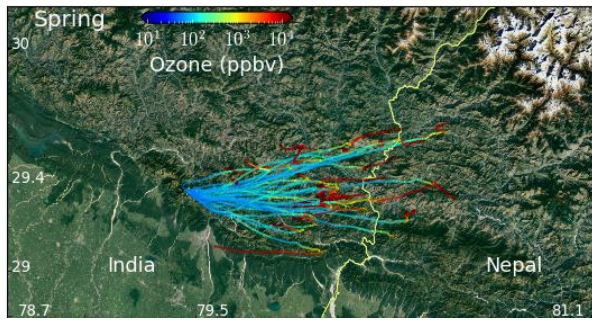
1198

Ozonesonde

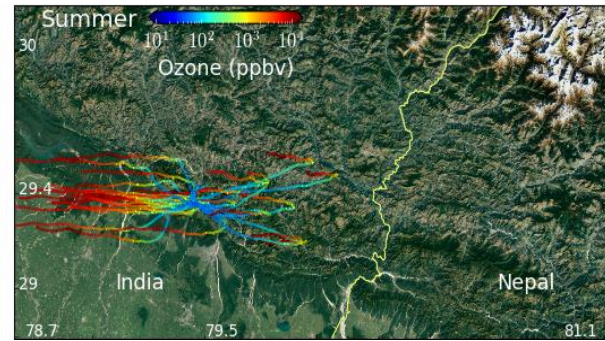
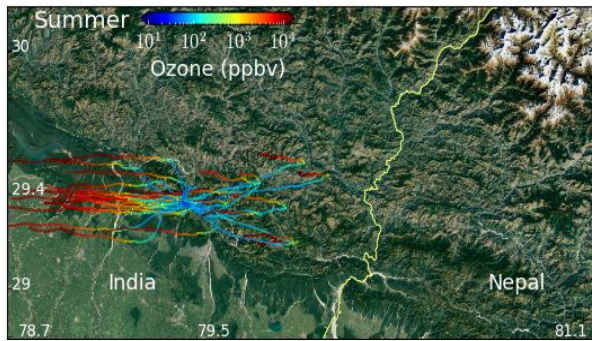
AIRS



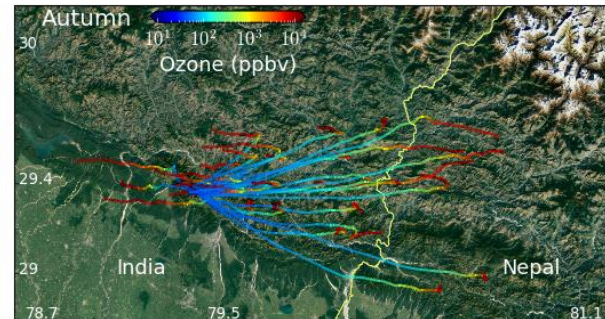
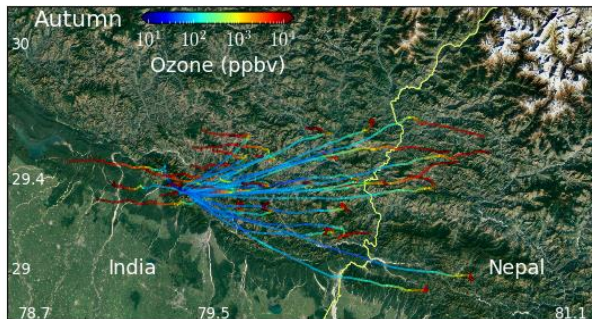
1199



1200



1201



1202

1203

1204

1205

1206

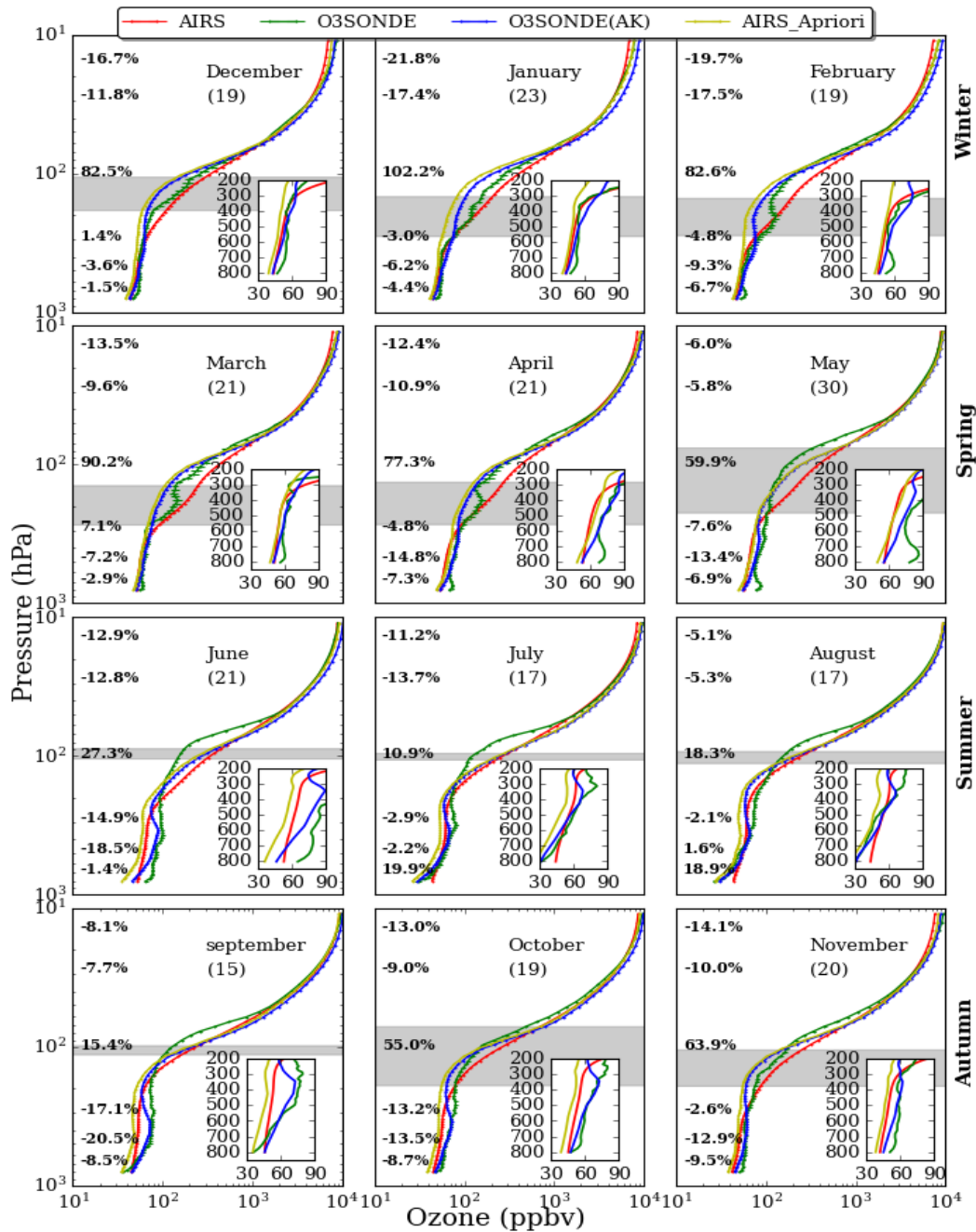
1207

1208

1209

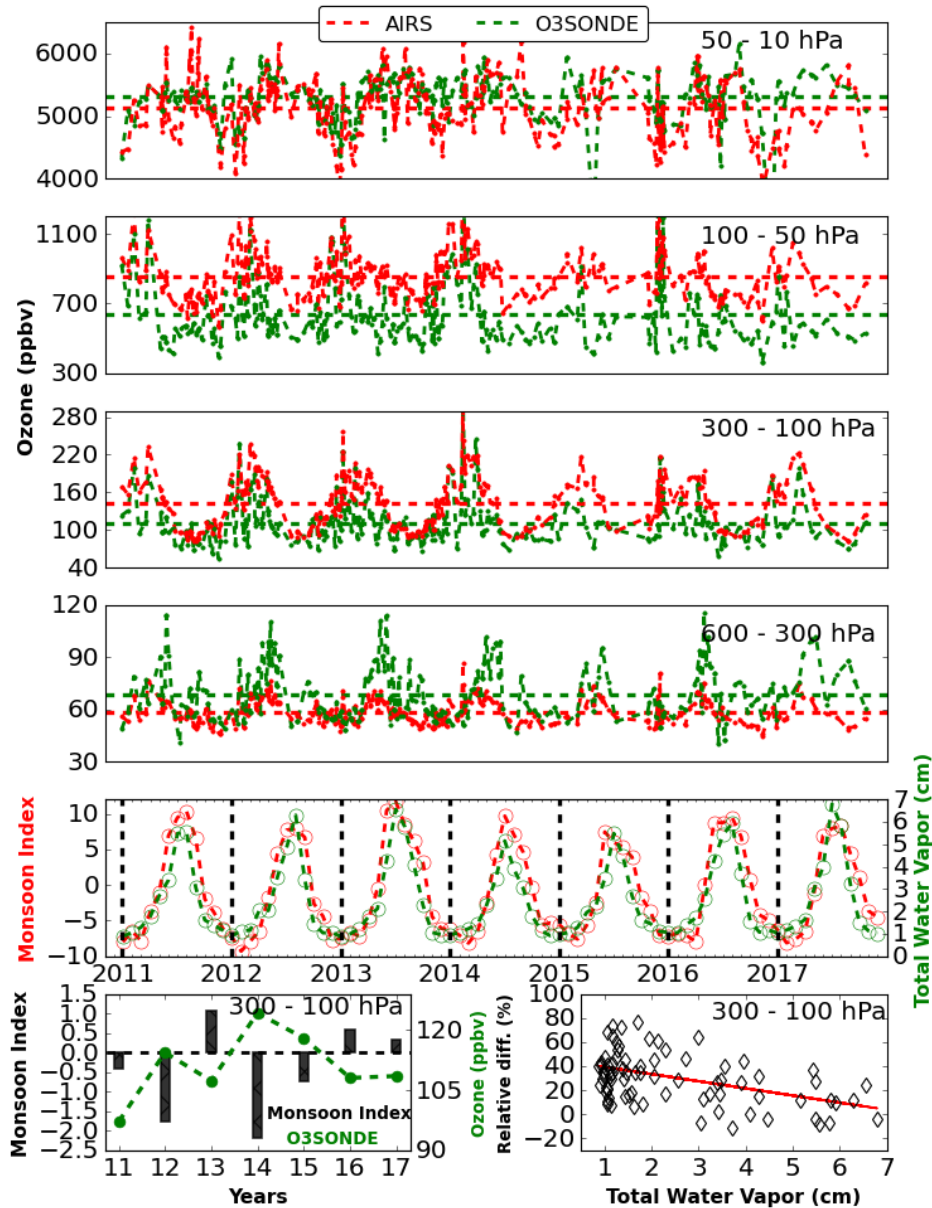
**Figure 4.** Spatial distribution of ozone using all ozone soundings (left) launched from ARIES, Nainital, India (Map from Google Earth, 2021) along with the balloon trajectories. Ozone spatial distribution from AIRS (right), following the balloon tracks, is also shown. It could be seen that the balloon reaches Nepal many times in the winter and autumn seasons.





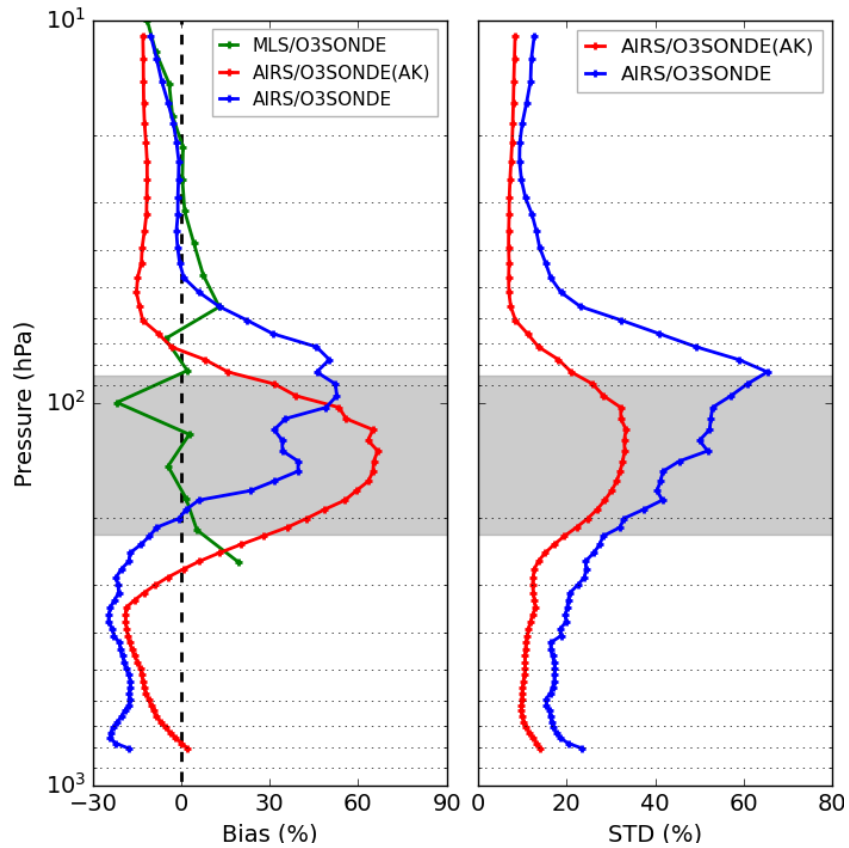
1210

1211 **Figure 5.** Monthly averaged (2011-2017) ozone profiles of ozonesonde, AIRS, ozonesonde(AK)  
 1212 and AIRS a-priori over Nainital in the central Himalaya. The percentage difference  $[(\text{AIRS} -$   
 1213  $\text{ozonesonde(AK)})/\text{ozonesonde(AK)}]*100$  at 706, 496, 300, 103, 29, and 14.4 hPa are also written  
 1214 at respective altitudes. The standard error corresponding to each profile is also shown with  
 1215 errorbars. The number of ozonesonde for different months is written in the bracket and grey shaded  
 1216 area shows the tropopause (mean $\pm$ sigma) from balloon-borne observations.



1217

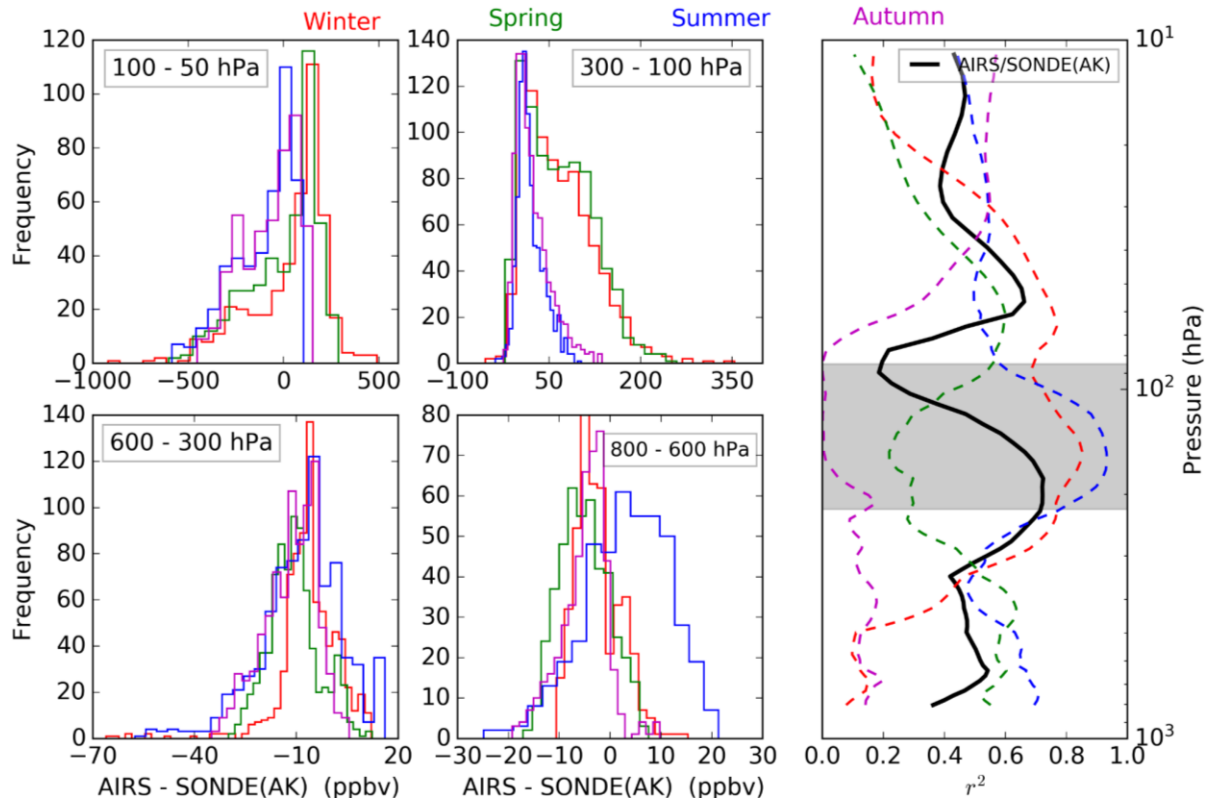
1218 **Figure 6.** Average variations in ozone mixing ratios at four defined layers, characterizing the  
 1219 middle stratosphere (50 - 10 hPa), the lower stratosphere (100 - 50 hPa), the upper troposphere  
 1220 (300 - 100 hPa), and the middle troposphere (600 - 300 hPa), respectively. The red and green dash  
 1221 horizontal lines show the average ozone mixing ratios in the defined layers from AIRS and  
 1222 ozonesonde, respectively, from 2011 to 2017. The monthly variation of the total column water  
 1223 vapor (cm) along with the monsoon index is also shown. (left lower most) The yearly average  
 1224 ozone from ozonesonde and monsoon index (bar plot) for different years and (right lower most)  
 1225 scattered plot of ozone relative difference (%)  $[(\text{AIRS}-\text{O3SONDE})/\text{O3SONDE}]*100$ , with total  
 1226 water vapor in the upper troposphere (300 - 100 hPa) is also shown.



1227

1228 **Figure 7.** Statistical error analysis (Bias and standard deviation) of AIRS retrieved ozone with  
 1229 ozonesonde and ozonesonde (AK) for collocated data of seven years (2011 - 2017). The Bias  
 1230 between collocated data of MLS (261 hPa - 10 hPa) and ozonesonde over Nainital during 2011 -  
 1231 2017 is also shown with the green profile. The grey shaded area shows the tropopause region from  
 1232 balloon-borne radiosondes observations.

1233



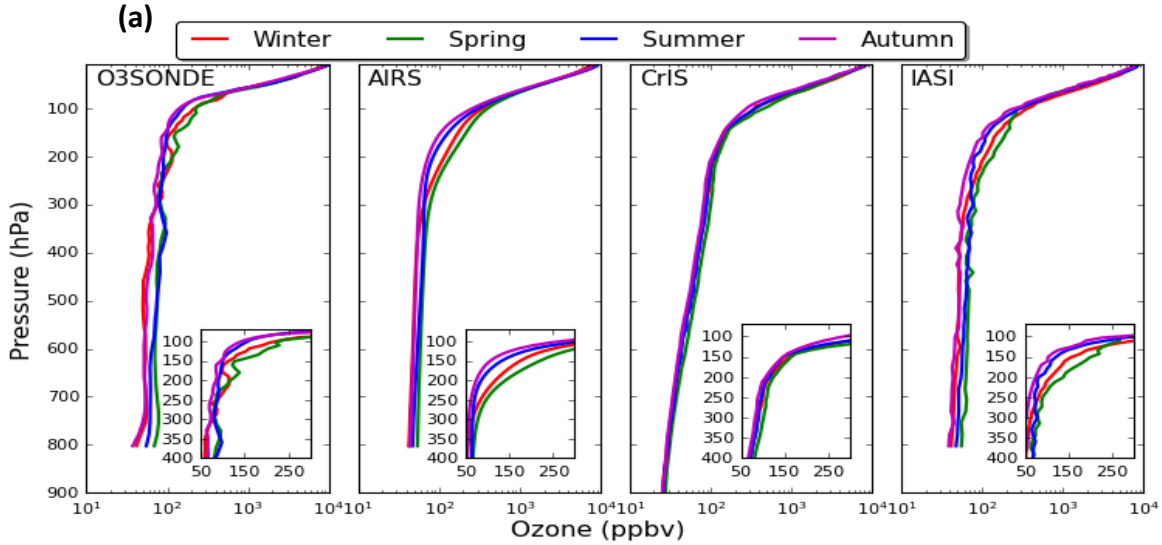
1234

1235 **Figure 8.** Histogram difference between AIRS ozone and ozonesonde(AK) in the four defined  
 1236 layers. The average correlation profiles between AIRS ozone and ozonesonde(AK) are shown on  
 1237 the right during winter (red), spring (green), summer-monsoon (blue), and autumn (magenta). The  
 1238 black line is for the entire data set. The grey shaded area shows the tropopause region from balloon-  
 1239 borne radiosondes observations.

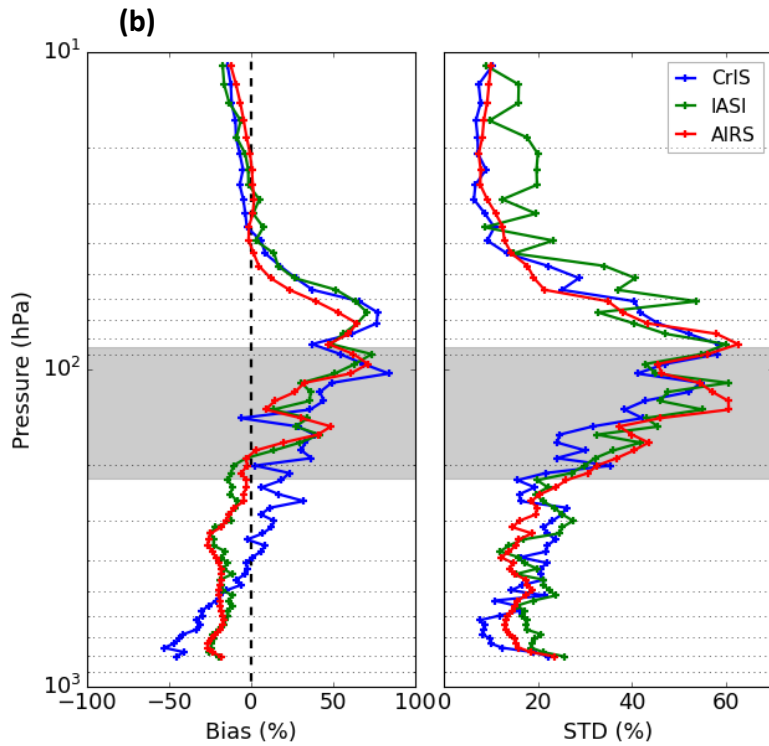
1240

1241

1242

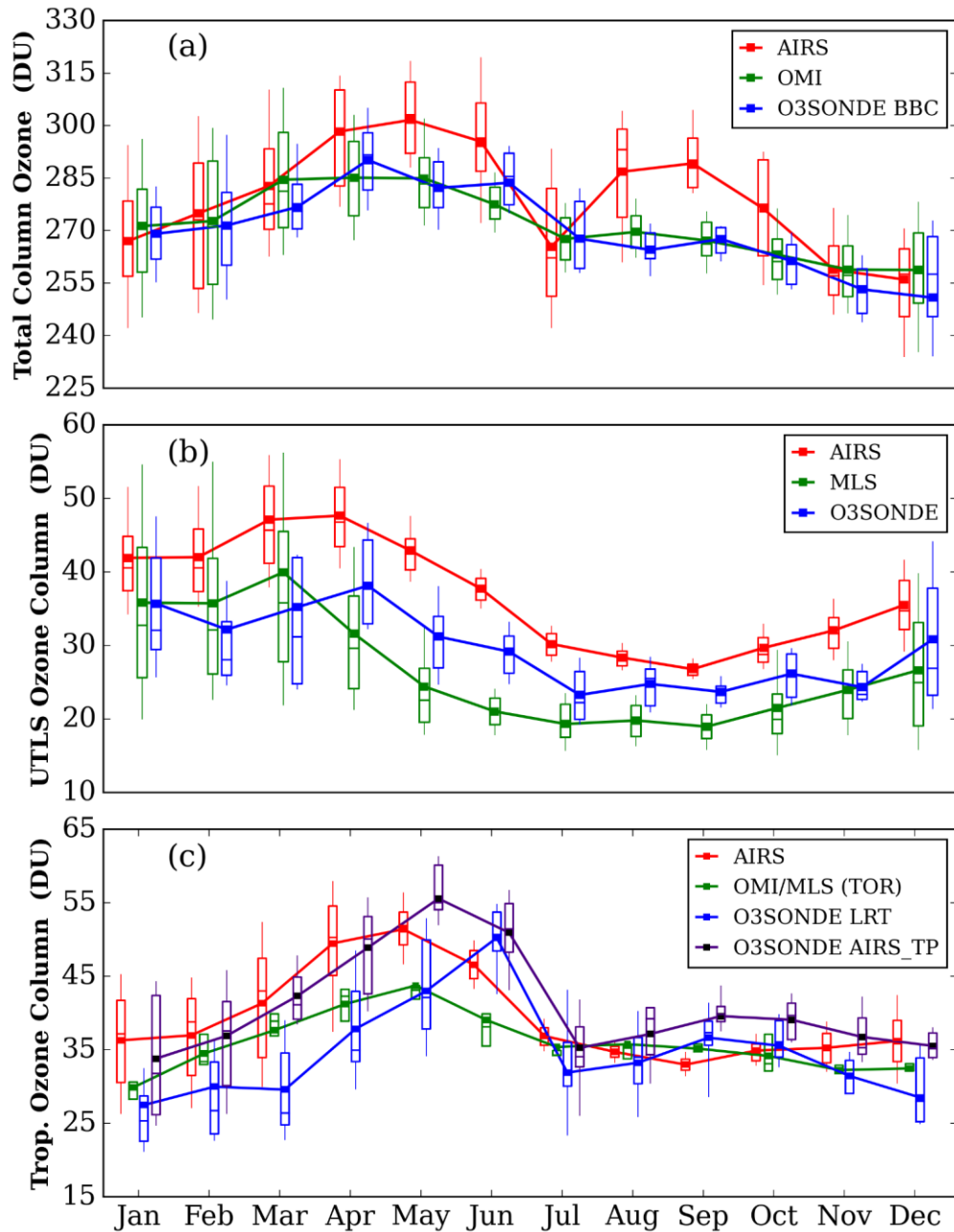


1243  
1244



1245

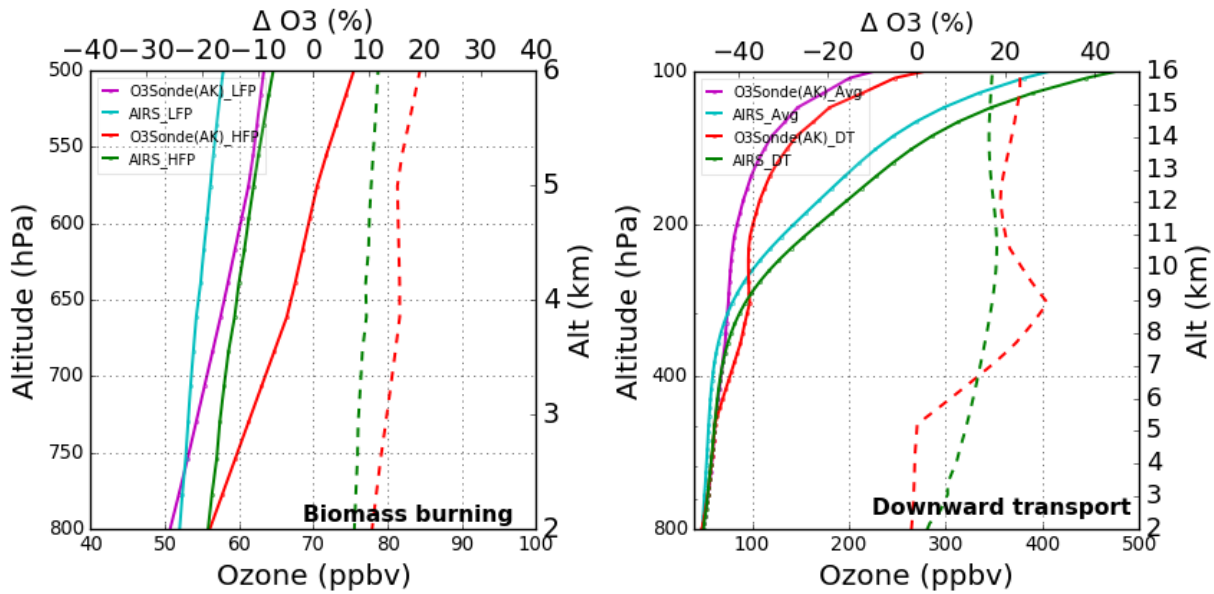
1246 **Figure 9.** (a) Seasonal ozone profiles of three IR satellites (IASI, AIRS, and CrIS) for a smaller  
1247 sample size (April 2014 to April 2015). The IASI and CrIS products are generated using the AIRS  
1248 heritage algorithm (NOAA) and only zero quality flags (QC=0) of retrieval are used. (b) Statistical  
1249 error analysis for the three IR satellites retrieved ozone without applying the averaging kernel  
1250 information. The grey shaded area shows the tropopause region from balloon-borne observations.



1251

1252 **Figure 10.** (a) Monthly average variations of total column ozone (TCO) for AIRS, OMI, and  
 1253 ozonesonde (Balloon Burst Climatology) over the central Himalaya for the 2011-2017 period. (b)  
 1254 Monthly average variation of UTLS ozone column for AIRS, MLS, and ozonesonde, over the  
 1255 central Himalayas for the 2011-2017 period. (c) Monthly average variations of tropospheric ozone  
 1256 column of AIRS, OMI/MLS (Tropospheric Ozone Residual), and ozonesonde (LRT - sonde lapse  
 1257 rate) over the central Himalayas for the 2011-2017 period. The ozonesonde tropospheric ozone  
 1258 column is also shown using AIRS tropopause (AIRS\_TP). In the box plot, the lower and upper  
 1259 edges of the boxes represent the 25th and 75th percentiles. The whiskers below and above are 10th  
 1260 and 90th percentiles.

1261



1262

1263 **Figure 11. (a)** Vertical ozone profiles of AIRS ozone and ozonesonde(AK) during low fire period

1264 (LFP) and high fire period (HEP). The solid lines correspond to ozone profiles while the dotted

1265 lines show a percentage increase in ozonesonde (red) and AIRS (green) profiles during biomass

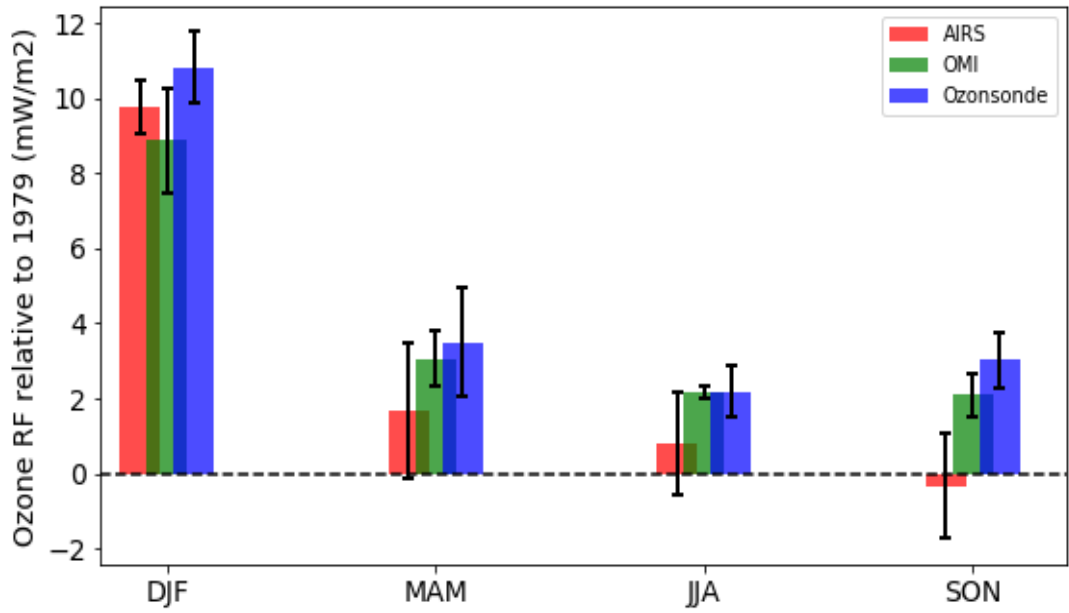
1266 burning events. **(b)** Vertical ozone profiles of AIRS ozone and ozonesonde(AK) during events of

1267 downward transport. The dotted line shows ozone enhancement during downward transport events.

1268

1269

1270



1271

1272 **Figure 12.** Seasonal average ozone UV radiative forcing (RF) relative to 1979 as calculated from  
 1273 ozonesonde, OMI, and AIRS total ozone data for the 2011 - 2017 period. Spreads correspond to  
 1274 one standard deviation.

1275